

1           **The *Fermi* GBM Gamma-Ray Burst Spectral Catalog:**  
2                           **Four Years Of Data**

3   David Gruber<sup>1,14</sup>, Adam Goldstein<sup>2</sup>, Victoria Weller von Ahlefeld<sup>1,3</sup>, P. Narayana Bhat<sup>2</sup>,  
4   Elisabetta Bissaldi<sup>4,5</sup>, Michael S. Briggs<sup>2</sup>, Dave Byrne<sup>6</sup>, William H. Cleveland<sup>7</sup>, Valerie  
5   Connaughton<sup>2</sup>, Roland Diehl<sup>1</sup>, Gerald J. Fishman<sup>8</sup>, Gerard Fitzpatrick<sup>6</sup>, Suzanne Foley<sup>6</sup>,  
6   Melissa Gibby<sup>9</sup>, Misty M. Giles<sup>9</sup>, Jochen Greiner<sup>1</sup>, Sylvain Guiriec<sup>10</sup>, Alexander J. van der  
7   Horst<sup>11</sup>, Andreas von Kienlin<sup>1</sup>, Chryssa Kouveliotou<sup>8</sup>, Emily Layden<sup>2</sup>, Lin Lin<sup>2,13</sup>, Charles  
8           A. Meegan<sup>2</sup>, Sinéad McGlynn<sup>6</sup> William S. Paciasas<sup>2</sup>, Vèronique Pelassa<sup>2</sup>,  
9   Robert D. Preece<sup>2</sup>, Arne Rau<sup>1</sup>, Colleen A. Wilson-Hodge<sup>8</sup>, Shaolin Xiong<sup>2</sup>, George Younes<sup>7</sup>  
10                           and Hoi-Fung Yu<sup>1</sup>

---

<sup>1</sup>Max-Planck-Institut für extraterrestrische Physik, Giessenbachstrasse 1, 85748 Garching, Germany

<sup>2</sup>University of Alabama in Huntsville, 320 Sparkman Drive, Huntsville, AL 35805, USA

<sup>3</sup>School of Physics and Astronomy, University of Edinburgh, James Clerk Maxwell Building, Mayfield Road, EH9 3JZ Edinburgh, United Kingdom

<sup>4</sup>Istituto Nazionale di Fisica Nucleare, Sezione di Trieste, I-34127 Trieste, Italy

<sup>5</sup>Dipartimento di Fisica, Università di Trieste, I-34127 Trieste, Italy

<sup>6</sup>School of Physics, University College Dublin, Belfield, Stillorgan Road, Dublin 4, Ireland

<sup>7</sup>Universities Space Research Association, 320 Sparkman Drive, Huntsville, AL 35805, USA

<sup>8</sup>Space Science Office, VP62, NASA/Marshall Space Flight Center, Huntsville, AL 35812, USA

<sup>9</sup>Jacobs Technology, Inc., Huntsville, Alabama

<sup>10</sup>NASA Goddard Space Flight Center, Greenbelt, MD 20771, USA

<sup>11</sup>Astronomical Institute, University of Amsterdam, Science Park 904, 1098 XH Amsterdam, The Netherlands

<sup>12</sup>Los Alamos National Laboratory, PO Box 1663, Los Alamos, NM 87545, USA

<sup>13</sup>Sabancı University, Faculty of Engineering and Natural Sciences, Orhanlı– Tuzla, İstanbul 34956, Turkey

<sup>14</sup>Planetarium Südtirol, Gummer 5, 39053 Karneid, Italy

**ABSTRACT**

12

13

In this catalog we present the updated set of spectral analyses of GRBs detected by the *Fermi* Gamma-Ray Burst Monitor (GBM) during its first four years of operation. It contains two types of spectra, time-integrated spectral fits and spectral fits at the brightest time bin, from 943 triggered GRBs. Four different spectral models were fitted to the data, resulting in a compendium of more than 7500 spectra. The analysis was performed similarly, but not identically to Goldstein et al. (2012). All 487 GRBs from the first two years have been re-fitted using the same methodology as that of the 456 GRBs in years three and four. We describe, in detail, our procedure and criteria for the analysis, and present the results in the form of parameter distributions both for the observer-frame and rest-frame quantities. The data files containing the complete results are available from the High-Energy Astrophysics Science Archive Research Center (HEASARC).

14

*Subject headings:* gamma rays: bursts — methods: data analysis

## 1. Introduction

15

16 During its first four years of operation, the *Fermi* Gamma-Ray Burst Monitor  
17 (GBM, Meegan et al. 2009) provided the scientific community with an enormous sample of  
18 Gamma-Ray Burst (GRBs) data, significantly expanding our understanding of the physical  
19 properties and characteristics of GRBs. In addition, discoveries of new and intriguing  
20 phenomena were associated with many individual GRBs (e.g. Ackermann et al. 2010;  
21 Guiriec et al. 2011; Ackermann et al. 2011; Axelsson et al. 2012; Guiriec et al. 2013).

22 Here, we present the second GBM GRB spectral catalog which will provide the most  
23 comprehensive resource of GRB spectral properties up to date. In order to be as complete  
24 and uniform as possible, our methodology follows closely, but is not identical to the  
25 procedures employed in the GRB Catalog from the Burst And Transient Source Experiment  
26 (BATSE) (Kaneko et al. 2006) and the first GBM GRB spectral Catalog (Goldstein et al.  
27 2012). We include representative spectral fits for all GBM bursts from the first four years  
28 of operation (July 14, 2008 to July 13, 2012).

29 For each GRB, we show two types of spectra: Time-integrated spectra (henceforth  
30 labelled  $F$  for *fluence*) and spectra at the brightest time bin (henceforth labelled  $P$  for  
31 *peak-flux*). A set of four empirical models was applied to the data in both cases. The  
32 selection of these model functions is based on tradition (Band et al. 1993; Kaneko et al.  
33 2006; Goldstein et al. 2012) and mathematical complexity. The signal-to-noise ratios in the  
34 data of GBM bursts rarely support models with more than four free parameters, which is  
35 why we resort to models with two, three or four free fit parameters and only in exceptional  
36 cases additive terms (e.g. a blackbody component Axelsson et al. 2012) can be added.  
37 Making use of the Castor statistics (Ackermann et al. 2011), we derive the best model for  
38 each GRB and present the distribution and characteristics of the model parameters.

39 This catalog is organized as follows: In Section 2 we present a short overview of the

40 GBM, in Section 3 we describe the methodology used in the production of this catalog,  
41 including detector selection, data types, energy selection and background fitting, and the  
42 source selection. We then offer a description of the spectral models used in this catalog in  
43 Section 4, present the spectral analysis methods in Section 5 and the results in Section 6.  
44 Finally, in Section 7 we conclude with a summary and a discussion.

## 45 2. *Fermi* GBM

46 The *Fermi*<sup>1</sup> Gamma-Ray Space Telescope was successfully launched on 2008 June 11  
47 into a Low Earth orbit (LEO) of  $\sim 565$  km altitude at an 25.6 degree inclination. Its  
48 payload comprises two instruments, the GBM and the Large Area Telescope (Atwood et al.  
49 2009, LAT). The goal of GBM is to augment the science return from *Fermi* with its prime  
50 objective being joint spectral and timing analyses of GRBs seen in common with the LAT. In  
51 addition, GBM provides near real-time burst locations which permit (i) the *Fermi* spacecraft  
52 to repoint the LAT towards the observed GRB and (ii) to perform follow-up observations  
53 with ground-based facilities. Compared to other high-energy spacecraft, the great advantage  
54 of GBM is its capability to observe the whole unocculted sky at any given time with a Field  
55 of View (FoV) of  $\geq 8$  sr and its very broad energy coverage. Therefore, along with GRBs,  
56 GBM offers great capabilities to observe all kinds of high-energy astrophysical phenomena,  
57 such as e.g., Solar Flares (e.g. Gruber et al. 2011a; Ackermann et al. 2012a), Soft Gamma  
58 Repeaters (SGRs, e.g. Lin et al. 2011; von Kienlin et al. 2012) and Terrestrial Gamma-Ray  
59 Flashes (TGFs, e.g. Briggs et al. 2013).

60 Designed to study the gamma-ray sky in the energy band of  $\sim 8$  keV–40 MeV, GBM is  
61 composed of twelve sodium iodide (NaI) and two bismuth germanate (BGO) scintillation

---

<sup>1</sup>Formerly known as the *Gamma-Ray Large Area Space Telescope* or GLAST

62 detectors. With a thickness of 1.27 cm and a diameter of 12.7 cm, the NaI crystals cover  
63 an energy range from 8 keV–1 MeV. They are oriented around the spacecraft such that the  
64 position of the GRB can be determined.

65 The two BGO crystals have a diameter and thickness of 12.7 cm, covering an energy  
66 range of 200 keV–40 MeV, and are located on opposite sides of the spacecraft so that at  
67 least one is illuminated from any direction. A source location is calculated in spacecraft  
68 coordinates and used in the production of the detector response matrices (see Section 5).

69 For more details on the GBM detectors and their calibration, refer to Meegan et al.  
70 (2009); Bissaldi et al. (2009); Paciesas et al. (2012).

### 71 3. Method

72 During the first four years of operation, GBM triggered on a total of 954 GRBs  
73 (von Kienlin et al. submitted), 943 of which are presented in this catalog. The remaining  
74 bursts are excluded due to a low accumulation of counts or a lack of spectral/temporal  
75 coverage. In order to deliver the most useful analysis to the community, we have attempted  
76 to make the method as systematic and uniform as possible; circumstances under which  
77 deviations were employed are clearly indicated. Details of the detector and data selection  
78 as well as the process used to fit the data are described in this section. Many of the  
79 criteria are adopted from the GBM Burst Catalog (Paciesas et al. 2012) and we have  
80 attempted to maintain this in all aspects. However, due to the nature of spectral analysis  
81 we demand stricter criteria to ensure that we have adequate signal in all energy channels.  
82 This effectively reduces the GRB sample from that used in the burst catalog.

83 We highlight that this catalog only presents the analysis of GRBs that *triggered* the  
84 GBM. There is a non-negligible amount of GRBs that did not trigger GBM whose temporal

85 and spectral properties are presented elsewhere (Gruber et al. 2012). These GRBs do not  
86 have different properties compared to the triggered GRB sample but simply occurred during  
87 times when the GBM triggering algorithm was switched off (e.g. when the spacecraft was  
88 at latitudes of high geomagnetic activity).

### 89 3.1. Detector Selection

90 The detector selection is consistent with Goldstein et al. (2012), i.e. a maximum of 3  
91 NaI detectors together with one BGO detector were used for the spectral analysis. Since  
92 the effective area (i.e. detection efficiency) of the NaI detectors decreases rapidly for high  
93 incidence angles (Bissaldi et al. 2009) only detectors with source angles  $\leq 60^\circ$  are used  
94 for the spectral analysis. In addition, it has been verified that the detectors were neither  
95 obstructed by the spacecraft nor by the solar panels of *Fermi*. However, due to small  
96 inaccuracies in the spacecraft mass model or location uncertainties, the blockage code does  
97 not always return a subset of detectors that is free from blockage. This is evident when  
98 the low-energy data deviate strongly from the fit model (Goldstein et al. 2012). When this  
99 occurs we remove these detectors from the selected sample. If more than 3 NaI detectors  
100 are qualified for the spectral fitting, the NaI detectors with the smallest source angles were  
101 used to avoid a fitting bias toward lower energies.

### 102 3.2. Data Types

103 GBM persistently records two different types of science data, called CTIME (fine  
104 time resolution, coarse spectral resolution of 8 energy channels) and CSPEC (coarse time  
105 resolution, full spectral resolution of 128 energy channels). CTIME (CSPEC) data have a  
106 nominal time resolution of 0.256 s (4.096 s) which is increased to 64 ms (1.024 s) whenever

107 GBM triggers on an event. After 600 s in triggered mode, both data types return to their  
108 non-triggered time resolution. The third and primary data type used in this catalog is the  
109 “Time Tagged Events” (TTE) which consist of individual events, each tagged with arrival  
110 time ( $2 \mu\text{s}$  precision), energy (128 channels) and detector number. The TTE data are  
111 generated and stored on-board in a continuously recycling buffer. When GBM enters trigger  
112 mode, the buffered pre-trigger TTE are transmitted as science data along with  $\sim 300$  s of  
113 post-trigger TTE.

114 For the purpose of this catalog, we choose a standard time binning of 1024 ms for  
115 bursts longer than 2 s in duration as defined by the burst  $T_{90}$  (Kouveliotou et al. 1993)  
116 presented in von Kienlin et al. (submitted) and 64 ms for bursts of duration 2 s and shorter.  
117 The time history of TTE typically starts at  $\sim 30$  s before trigger and extends to  $\sim 300$  s  
118 after trigger. This TTE data time span is adequate for the analysis of most GRBs. For  
119 GRBs that have evident precursors or emissions that last more than 300 s after trigger, we  
120 use the CSPEC data, which extend  $\sim 4000$  s before and after the burst for triggered events.  
121 CSPEC data were used for 76 GRBs in this catalog.

### 122 **3.3. Energy Selection and Background Fitting**

123 With the optimum subset of detectors selected, the best time and energy selections  
124 are chosen to fit the data. The available and reliable energy channels in the NaI detectors  
125 lie between  $\sim 8$  keV and  $\sim 1$  MeV. This selection excludes the overflow channel at high  
126 energies and those channels  $< 8$  keV where the transmission of gamma-rays is poor due to  
127 the silicone pad in front of the NaI crystal and the Multi Layer Insulation (MLI) around  
128 the detectors (Bissaldi et al. 2009). We perform a similar selection to the BGO detector  
129 for each burst, selecting channels between  $\sim 300$  keV and  $\sim 38$  MeV. We select enough pre-  
130 and post-burst data to sufficiently model the background and fit a single energy dependent

131 polynomial (choosing up to 4<sup>th</sup> order) to the background. For each detector the time  
132 selection and polynomial order are varied until the  $\chi^2$  statistic map over all energy channels  
133 is minimized, resulting in an adequate background fit. This approach is rather subjective  
134 in that it is dependent on the observer’s choice of the background intervals. In the future,  
135 it may be advantageous to implement more objective background selection methods such  
136 as the “direction dependent background fitting (DBBD)” method presented in Szécsi et al.  
137 (2012).

### 138 3.4. Source Selection

139 Knowing the background model, the background-subtracted count rates are summed  
140 over all NaI detectors for a given burst to produce a single GRB count light curve. Using  
141 this light curve, only time bins (1.024 s for long burst and 64 ms for short bursts) with a  
142 signal-to-noise ratio greater or equal to 3.5 were selected, in agreement with Goldstein et al.  
143 (2012). This time selection is then applied to all detectors for a given burst.

144 This criterion ensures that there is adequate signal to successfully perform a spectral fit  
145 and constrain the parameters of the fit. This does however eliminate some faint bursts from  
146 the catalog sample (i.e., those with no time bins with signal above 3.5 sigma). While the  
147 possibility remains that not all signal from the GRB was selected, this method nevertheless  
148 provides the most objective way to obtain a selection of intrinsic GRB counts as including  
149 less significant bins would only increase the uncertainty in the measurements.

150 This selection is what we refer to as the  $F$  selection, since it is a time-integrated  
151 selection and the derived photon and energy fluences are representative of but not equal  
152 to the fluence over the total duration of the burst. We draw attention to the fact that  
153 time bins with a signal-to-noise ratio less than 3.5, which were not included in the fitting

154 process, also contribute to the photon and energy fluence. For more than 80 % of the GRBs  
 155 in the catalogue the ratio of count fluence (without the intervals with  $\text{SNR} < 3.5$ ) vs the  
 156 total counts (with the intervals with  $\text{SNR} < 3.5$ ) is larger than 0.8. So while there are some  
 157 bursts for which the fluence can be considerably underestimated, the other option would be  
 158 to overestimate the fluence of those bursts by including background that contaminates the  
 159 spectral fits.

160 The other selection performed is a 1.024 s peak photon flux selection for long bursts  
 161 ( $T_{90} > 2$  s) and 64 ms peak count rate flux selection for short bursts ( $T_{90} \leq 2$  s). This  
 162 selection is made by adding the count rates in the NaI detectors again and selecting the  
 163 single bin of signal with the highest background-subtracted count rate. This selection is a  
 164 snapshot of the energetics at the most intense part of the burst and is depicted as the  $P$   
 165 selection.

166 Figure 1 shows the distribution of accumulation times used for the fitting process  
 167 based on the signal-to-noise selection criteria. The distribution of accumulation times  
 168 reported is similar to the observed emission time of the burst, excluding quiescent periods,  
 169 (e.g. Mitrofanov et al. 1999) and peaks at 0.26 s and  $\sim 15$  s for short and long GRBs,  
 170 respectively. The dividing duration time scale between the two classes of GRBs is  $\sim 1.27$  s  
 171 and is, as expected from the employed source selection methodology, somewhat smaller  
 172 than the canonical 2 s (Kouveliotou et al. 1993). Figure 1 also includes the comparisons  
 173 of the model photon fluence and model photon flux compared to the accumulation time.  
 174 In both cases two specific regions are visible for long and short GRBs. In addition,  
 175 there is a clear correlation between the photon fluence (flux) and accumulation time in  
 176 Figure 1(b) and Figure 1(c) shows a relationship indicating the existence of two different  
 177 burst groups, similar to the ones delineated by the hardness–duration relationship found by  
 178 Kouveliotou et al. (1993).

179

## 4. Models

180 We chose four spectral models to fit the spectra of GRBs in our selection sample. These  
 181 models include a single power law (PL), Band’s GRB function (BAND), an exponential  
 182 cut-off power-law (COMP), and a smoothly broken power law (SBPL). All models are  
 183 formulated in units of photon flux with energy ( $E$ ) in keV and multiplied by a normalization  
 184 constant  $A$  ( $\text{ph s}^{-1} \text{cm}^{-2} \text{keV}^{-1}$ ). Below we describe each model and its features in detail.

185

### 4.1. Power-Law Model

186 The single power law with two free parameters is defined as

$$f_{\text{PL}}(E) = A \left( \frac{E}{E_{\text{piv}}} \right)^{\lambda} \quad (1)$$

187 where  $A$  is the amplitude and  $\lambda$  is the spectral index. The pivot energy ( $E_{\text{piv}}$ ) normalizes  
 188 the model to the energy range under consideration and helps reduce cross-correlation of  
 189 other parameters. In all cases,  $E_{\text{piv}}$  is held fixed at 100 keV. While most GRBs exhibit a  
 190 spectral break in the GBM passband, some GRBs are too weak to adequately constrain this  
 191 break in the fits. These bursts are well fit by the single power-law.

192

### 4.2. Band’s GRB function

193 Band’s GRB function (Band et al. 1993) has become the standard for fitting GRB  
 194 spectra, and therefore we include it in our analysis:

$$f_{\text{BAND}}(E) = A \begin{cases} \left(\frac{E}{100 \text{ keV}}\right)^\alpha \exp\left[-\frac{(\alpha+2)E}{E_{\text{peak}}}\right], & E < \frac{(\alpha-\beta) E_{\text{peak}}}{\alpha+2} \\ \left(\frac{E}{100 \text{ keV}}\right)^\beta \exp(\beta - \alpha) \left[\frac{(\alpha-\beta)E_{\text{peak}}}{100 \text{ keV} (\alpha+2)}\right]^{\alpha-\beta}, & \\ E \geq \frac{(\alpha-\beta) E_{\text{peak}}}{\alpha+2} \end{cases}, \quad (2)$$

195 The four free parameters are the amplitude,  $A$ , the low and high energy spectral indices,  $\alpha$   
 196 and  $\beta$ , respectively, and the  $\nu F_\nu$  peak energy,  $E_{\text{peak}}$ . This function is essentially a smoothly  
 197 broken power law with a curvature defined by its spectral indices. The low-energy index  
 198 spectrum is a power law only asymptotically.

### 199 4.3. Comptonized Model

200 The Comptonized model is an exponentially cutoff power-law, which is a subset of the  
 201 Band function in the limit that  $\beta \rightarrow -\infty$ :

$$f_{\text{COMP}}(E) = A \left(\frac{E}{E_{\text{piv}}}\right)^\alpha \exp\left[-\frac{(\alpha+2) E}{E_{\text{peak}}}\right] \quad (3)$$

202 The three free parameters are the amplitude  $A$ , the low energy spectral index  $\alpha$  and  $E_{\text{peak}}$ .  
 203  $E_{\text{piv}}$  is again fixed to 100 keV, as for the power law model.

### 204 4.4. Smoothly Broken Power-Law

205 The final model that we consider in this catalog is a broken power-law characterized by  
 206 one break with flexible curvature and is able to fit spectra with sharp or smooth transitions  
 207 between the low and high energy power laws. This model, first published in Ryde (1999),  
 208 where the logarithmic derivative of the photon flux is a continuous hyperbolic tangent, has

209 been re-parametrized (Kaneko et al. 2006) as given below:

$$f_{\text{SBPL}}(E) = A \left( \frac{E}{E_{\text{piv}}} \right)^b 10^{(a-a_{\text{piv}})} \quad (4)$$

210 where

$$a = m\Delta \ln \left( \frac{e^q + e^{-q}}{2} \right),$$

$$a_{\text{piv}} = m\Delta \ln \left( \frac{e^{q_{\text{piv}}} + e^{-q_{\text{piv}}}}{2} \right), \quad (5)$$

$$q = \frac{\log(E/E_b)}{\Delta}, \quad q_{\text{piv}} = \frac{\log(E_{\text{piv}}/E_b)}{\Delta},$$

$$m = \frac{\lambda_2 - \lambda_1}{2}, \quad b = \frac{\lambda_1 + \lambda_2}{2}.$$

211 In the above relations, the low- and high-energy power law indices are  $\lambda_1$  and  $\lambda_2$  respectively,  
 212  $E_b$  is the break energy in keV, and  $\Delta$  is the break scale in decades of energy. The break  
 213 scale is independent and not coupled to the power law indices as for the Band function,  
 214 and represents an additional degree of freedom. However, Kaneko et al. (2006) found that  
 215 an appropriate value for  $\Delta$  for GRB spectra is 0.3, therefore we fix  $\Delta$  at this value. In  
 216 addition, we tested the behavior of  $\Delta$  for some bright GRBs by letting it vary during the  
 217 fit process. The results of this study are presented in Section 6.

218 We choose to fit these four different functions because the measurable spectrum of  
 219 GRBs is dependent on intensity. Less intense bursts (in the observer frame) provide less  
 220 data to support a large number of parameters. This may appear obvious, but it allows us  
 221 to determine why in many situations a particular empirical function provides a poor fit,  
 222 while in other cases it provides an accurate fit. For example, the energy spectra of GRBs  
 223 are normally well fit by two smoothly joined power laws. For particularly bright GRBs, the

224 BAND and SBPL functions are typically an accurate description of the spectrum, while for  
225 weaker bursts the COMP function is most appropriate. Bursts that have signal significance  
226 on the order of the background fluctuations do not have a detectable distinctive break in  
227 their spectrum and so the power law is the most appropriate function.

## 228 5. Data Analysis

229 The spectral analysis of all bursts was performed using RMfit, version 4.0rc1. RMfit  
230 employs a modified, forward-folding Levenberg-Marquardt algorithm for spectral fitting  
231 which means that the aforementioned models are used as trial source spectra which are  
232 converted to predicted detector count histograms. These histograms, in turn, are then  
233 compared to the actual, observed data.

234 In order to work properly, a method must be established to associate the energy  
235 deposited in the detectors to the energy of the detected photons, which depends on  
236 effective area and the angle of the detector to the incoming photons. We use detector  
237 response matrices (DRMs) to convert the photon energies into detector channel energies.  
238 DRMs contain information about the effective area of the detector, effects of the angular  
239 dependence of the detector efficiency, partial energy deposition in the detector, energy  
240 dispersion and nonlinearity of the detector and, finally, atmospheric and spacecraft  
241 scattering of photons into the detector. Therefore, DRMs are functions of photon energy,  
242 measured energy, the direction to the source (with respect to the spacecraft) and the  
243 orientation of the latter with respect to the Earth. The response matrices for all GRBs  
244 in the catalog were made using GBMRSP v2.0 of the response generator and version 2  
245 of the GBM DRM database, and all responses employ atmospheric response modeling to  
246 correct for atmospheric scattering. In particular, we use RSP2 files, which contain multiple  
247 DRMs based on the amount of slew the spacecraft experiences during the burst. A new

248 DRM is calculated for every  $2^\circ$  of slew, changing the effective area of each detector based  
249 on its angle to the source. These DRMs are then all stored in a single RSP2 file for each  
250 detector. During the fitting process, each DRM is weighted by the counts fluence through  
251 the detector during each  $2^\circ$  slew segment.

252 At all times, the Castor C-Statistic (C-Stat), which is a modified log likelihood statistic  
253 based on the Cash parametrization (Cash 1979) is used in the model-fitting process as  
254 a figure of merit to be minimized. This statistic is preferable over the more traditional  
255  $\chi^2$  statistic minimization because of the non-Gaussian counting statistics present when  
256 dividing the energy spectra of GBM GRBs into 128 channels. The drawback of this statistic  
257 is that it does not provide an estimation of the goodness-of-fit, since no standard probability  
258 distribution for likelihood statistics exists. Normally, the goodness-of-fit must be estimated  
259 for the model in use. This is usually done by simulating the model many times in order  
260 to calculate a test statistic, C-Stat in this case, for each fake model of each dataset. The  
261 observed value of the test statistic is then compared to the constructed fake test statistic  
262 distribution. This would allow to reject a model with a certain level of confidence. However,  
263 performing these kind of simulations is unfeasible for such a large sample of GRBs. In  
264 addition, any goodness-of-fit method can never provide a probability that any given model  
265 is the adequate representation of the burst emission, i.e. the correct model. Therefore,  
266 we refrain from performing extensive goodness-of-fit tests and present the fit parameters  
267 for each model fit, independent of the goodness-of-fit. As we only apply four different  
268 models, it can be instructive to study the fit parameters even if the model is not a perfect  
269 representation of the data. We do, however, apply additional selection criteria and employ  
270 cuts to define a GOOD and BEST sample of the obtained fit results. These are explained  
271 in the following subsections.

272 Finally, we caution the reader that the  $1\sigma$  errors reported in this catalog are of

273 statistical nature only. Systematic effects were not considered which generally are  
 274 non-negligible. For example, for weak events a different selection of *on* and *off* intervals for  
 275 the background fitting can have effects as large as 30% for the final reported value of  $E_{\text{peak}}$   
 276 (see also Collazzi et al. 2011).

### 277 5.1. The GOOD sample

278 We classify fitted burst models as GOOD if the parameter error of *all* model parameters  
 279 is within certain limits. This is a more conservative approach compared to Kaneko et al.  
 280 (2006) and Goldstein et al. (2012) who only required the error of the parameter of interest  
 281 to be within given limits. The motivation behind this new approach is to show parameter  
 282 values of models which are *globally* well-constrained, rather than basing interpretations on  
 283 constrained parameters of overall poorly constrained models. We simultaneously require for  
 284 the low-energy power law an error less than 0.4, for high-energy power law indices an error  
 285 less than 1.0 and for all other parameters we require a relative error of 0.4 or less. These  
 286 criteria are an arbitrary choice but are in line with other GRB catalogs (Kaneko et al. 2006;  
 287 Goldstein et al. 2012). Applying these criteria, the number of bursts that classify as GOOD  
 288 for each employed model can be seen in Table 2. We draw the reader’s attention to the fact  
 289 that for many GRBs there can be several models which qualify as GOOD.

### 290 5.2. The BEST sample

291 In addition, we define a BEST sample in order to determine which of the GOOD models  
 292 is the best representation of the burst emission. Besides the necessity of having constrained  
 293 parameters – already required for the GOOD sample – we compare the difference in C-Stat  
 294 ( $\Delta\text{C-Stat}$ ) per degree of freedom between the various models. In order to assess if a

295 statistically more complex model, i.e. a model with more free fit parameters (hypothesis  
 296 H1) is preferred over a simpler model (null hypothesis H0) according to its difference in  
 297 C-Stat, we created a set of  $5 \times 10^4$  synthetic GRB spectra using the fit parameters of H0,  
 298 obtained from the fit to the real data, as source counts. Similarly, the background counts  
 299 of the synthesized spectra are estimated from the real data. The input source counts are  
 300 then folded through the detector response matrix (DRM). Finally, Poisson noise was added  
 301 to the sum of the source and background counts. The synthetic spectra were then fitted  
 302 with both models, adding Poisson fluctuations to each energy channel of the background  
 303 spectrum during the fit process.

304 Integrating the  $\Delta$ C-Stat distribution from 0 to 99.73% (i.e. a  $3\sigma$  confidence interval)  
 305 we identified a critical  $\Delta$ C-Stat<sub>crit</sub>. If the  $\Delta$ C-Stat observed in the real data exceeds this  
 306 critical value, then the null hypothesis is rejected and the statistically more complex model  
 307 is preferred.

308 As the full GRB sample contains nearly 1000 GRBs doing the aforementioned analysis  
 309 for all bursts is not feasible. We used four typical bursts which are located in four energy  
 310 fluence classes, separated by one order of magnitude. These bursts are GRB 120608.489,  
 311 GRB 110227.240, GRB 120129.580 and GRB 120526.303 with an energy fluence [10 keV –  
 312 1 MeV] of  $5.2 \times 10^{-7}$  erg cm<sup>-2</sup>,  $1.9 \times 10^{-6}$  erg cm<sup>-2</sup>,  $5.8 \times 10^{-5}$  erg cm<sup>-2</sup>,  $1.3 \times 10^{-4}$  erg cm<sup>-2</sup>,  
 313 respectively.

314 For each of the aforementioned GRBs, we created a PL vs COMP and a COMP vs BAND  
 315 distribution and determined the  $\Delta$ C-Stat<sub>crit</sub> for each model comparison. To assess which of  
 316 the four models qualifies for the BEST sample we used the critical values as a function of  
 317 fluence. For the comparison between the BAND and the SBPL such simulations were not  
 318 necessary, as both functions have the same number of degrees of freedom. Therefore, the  
 319 model with the lower C-Stat value was used.

320 As there is no observable correlation between  $\Delta\text{C-Stat}_{\text{crit}}$  and the energy fluence (see  
 321 Table 1) we use the average  $\Delta\text{C-Stat}_{\text{crit}}$  value, for the model selection of all bursts, i.e. for  
 322 PL vs COMP we use  $\Delta\text{C-Stat}_{\text{crit}} = 8.58$  and for COMP vs BAND we use  $\Delta\text{C-Stat}_{\text{crit}} = 11.83$

323 The key idea for the BEST parameter sample is to obtain the best estimate of the  
 324 observed properties of GRBs. By using model comparison, the preferred model is selected,  
 325 and the parameters are reviewed for that model. The models contained herein and in most  
 326 GRB spectral analyses are empirical models, based only on the data received; therefore the  
 327 data from different GRBs tend to support different models. Perhaps it will be possible to  
 328 determine the physics of the emission process by investigating the tendencies of the data to  
 329 support a particular model over others. This is the motivation to provide a sample that  
 330 contains the best picture of the global properties of the data, that prompts the investigation  
 331 of the BEST sample.

332 Applying the BEST criteria we are left with 941 GRBs for the fluence spectra and  
 333 932 GRBs for the  $P$  spectra (see again Table2). These numbers are smaller than the total  
 334 number of GRBs in this catalog (943). This is due to the fact that for some bursts the  
 335 spectral fit did not converge properly and these bursts have been excluded from the BEST  
 336 sample.

337 In Table 2 we present the composition of models for the BEST samples. From this  
 338 table, it is apparent that the  $F$  spectral fits strongly favors the COMP model over the others  
 339 in over half of all GRBs. The BAND and SBPL are favored by only few GRBs in the catalog.  
 340 It should be noted that the number of GRBs best fit by PL increases in the  $P$  selection  
 341 mainly due to the fact that the smaller statistics from the short integration time are unable  
 342 to support a model more complex than the PL.

### 5.3. The redshift sample

343

344 In addition to the BEST sample, we form a sample of GRBs with known redshift<sup>2</sup>  
 345 (determined either spectroscopically or photometrically) to investigate the rest-frame  
 346 properties of the GRBs (see e.g. Gruber et al. 2011b). The redshift distribution of the  
 347 GBM GRBs with known redshift to date is shown in Figure 2. The redshift sample contains  
 348 45 triggered GRBs with an additional 3 untriggered GRBs (Gruber et al. 2012) for the  $F$   
 349 spectral fits. As apparent from Figure 2, the sample of GBM GRBs with measured redshift  
 350 is compatible with the full sample of GRBs with redshift and therefore it can be concluded  
 351 that the GBM observations do not introduce a new bias for bursts with measured redshift.  
 352 This is also confirmed by an KS-test which yields a probability of 98 % that the two  
 353 distributions are drawn from the same population.

354

At all times the cosmological parameters obtained from the *Planck* mission  
 355 (Planck Collaboration 2005) with  $H_0 = 67.3 \text{ km s}^{-1} \text{ Mpc}^{-1}$ ,  $\Omega_m = 0.315$  (Ade et al. 2013)  
 356 were used for this analysis.

357

## 6. Results

358

### 6.1. Time-integrated $F$ spectral fits

359

The time-integrated spectral distributions depict the overall emission properties and  
 360 do not take into account any spectral evolution. The low-energy indices, as shown in Figure  
 361 3, are distributed about a  $-1.1$  power law typical of most GRBs. Up to 17% of the BEST  
 362 low-energy indices exceed  $\alpha > -2/3$ , violating the synchrotron “line-of-death” (Preece et al.  
 363 1998b), while an additional 18% of the indices are  $\alpha < -3/2$ , violating the synchrotron

---

<sup>2</sup>[www.mpe.mpg.de/~jcg/grbgen.html](http://www.mpe.mpg.de/~jcg/grbgen.html)

364 cooling limit. The high-energy indices in Figure 4 peak at a slope of about  $-2.1$  and have a  
 365 long tail toward steeper indices. Note that very steep high-energy indices in the distribution  
 366 of all high-energy index values indicate that the spectrum of these GRBs mimics closely a  
 367 COMP model, which is equivalent to a BAND function with a high-energy index of  $-\infty$ . A  
 368 significant fraction of BAND model fits results in a high-energy power-law index  $\beta > -2$   
 369 which would indicate a divergent energy flux at high energies. However, it was pointed out  
 370 by Ackermann et al. (2012b) that the inclusion of *Fermi*/LAT upper limits in the fitting  
 371 process results in considerably steeper (softer) high-energy power-law indices. The median  
 372 value decreased from  $\beta \sim -2.2$  from the GBM-only fits to  $\beta \sim -2.5$  for the GBM and LAT  
 373 joint spectral fits. Indeed, not a single case of their sample had a high-energy power-law  
 374 index  $> -2$  after LAT data had been included. Ackermann et al. (2012b) conclude that  
 375 intrinsic spectral breaks and/or softer-than-measured high-energy spectra must be fairly  
 376 common in the GRB population in order to explain the lack of LAT-detected GRBs.

377 The comparison of the single power law index to the low- and high-energy indices  
 378 makes evident that the simple power law index is averaged over the break energy, resulting  
 379 in an index that is on average steeper than the low-energy index, yet shallower than the  
 380 high-energy index. In addition, the lack of power-law indices steeper than  $-2$  suggest  
 381 that GBM does not detect a population of GRBs with low  $E_{\text{peak}}$ . If a burst had a Band  
 382 spectrum with  $E_{\text{peak}}$  near or below the GBM energy threshold a single power-law fit should  
 383 have an index smaller than  $-2$ .

384 We also show in Figure 5 the difference between the time-integrated low- and  
 385 high-energy spectral indices,  $\Delta S = (\alpha - \beta)$ . This quantity is useful since the synchrotron  
 386 shock model (SSM) makes predictions of this value in a number of cases (Preece et al.  
 387 2002) and the power-law index,  $p$ , of the electron distribution can be inferred from  $\Delta S$ .  
 388 The distributions of  $\Delta S$  obtained from the GOOD and BEST  $F$  spectral fits are consistent

389 with the time-resolved results in Preece et al. (2002), as well as the time-integrated results  
 390 in Kaneko et al. (2006), peaking at  $\Delta S \sim 1$  with a median value of 1.25.

391 In Figure 6 and Figure 7, we show the distributions for the break energy,  $E_b$  and the  
 392 peak of the power density spectrum,  $E_{\text{peak}}$ , respectively.  $E_b$  is the energy at which the low-  
 393 and high-energy power laws are joined, which is not necessarily representative of the  $E_{\text{peak}}$ .  
 394 However, one can easily derive  $E_b$  from the BAND  $E_{\text{peak}}$  values following Kaneko et al.  
 395 (2006). The  $E_b$  for the GOOD SBPL and BAND fits has a clustering about 120 keV  
 396 spanning roughly two orders of magnitude. The  $E_b$  distribution for the BEST sample is  
 397 skewed to slightly smaller values than the GOOD sample implying that the SBPL is more  
 398 likely to be statistically preferred if  $E_b$  is low. The GOOD and BEST  $E_{\text{peak}}$  distributions  
 399 all generally peak around 150 - 200 keV and cover just over two orders of magnitude, which  
 400 is consistent with previous findings (Mallozzi et al. 1995; Lloyd et al. 2000) from BATSE.  
 401 As discussed in Kaneko et al. (2006), although the SBPL is parametrized with  $E_b$ , the  $E_{\text{peak}}$   
 402 can be derived from the functional form. We have calculated the  $E_{\text{peak}}$  for all bursts with  
 403 low-energy index shallower than -2 and high-energy index steeper than -2.

404 The overall distribution of  $E_{\text{peak}}$  is similar to that found using the BATSE Large Area  
 405 Detectors, which had a much smaller bandwidth and larger collecting area. This would  
 406 seem to indicate that it is unlikely a hidden population to be undiscovered within the 10  
 407 keV - 40 MeV range which is in line with the results by Harris & Share (1998).

408 The value of  $E_{\text{peak}}$  can strongly affect the measurement of the low-energy index of the  
 409 spectrum, as shown in Figure 8. A general trend appears to show that spectra with smaller  
 410  $E_{\text{peak}}$  values also have smaller values of the low-energy power-law index. This is due to the  
 411 fact that when  $E_{\text{peak}}$  is close to the instrument's lower energy sensitivity limit,  $\alpha$  has not  
 412 yet reached its asymptotical value and is thus, on average, softer than it is in reality. In  
 413 addition, smaller  $E_{\text{peak}}$  values tend to increase the uncertainty in the measurement of the

414 low-energy index, mostly due to the fact that a spectrum with a low  $E_{\text{peak}}$  will exhibit most  
 415 of its curvature near the lower end of the instrument bandpass.

416 It is of interest to study the difference in the value of  $E_{\text{peak}}$  between the BAND and  
 417 COMP functions since they are the two main functions used to study GRB spectra, and  
 418 COMP is a special case of BAND. To study the relative deviation between the two values  
 419 we calculate a statistic based on the difference between the values and taking into account  
 420 their  $1\sigma$  errors. This statistic can be calculated by

$$\Delta E_{\text{peak}} = \frac{|E_{\text{peak}}^C - E_{\text{peak}}^B|}{\sigma_{E_{\text{peak}}}^C + \sigma_{E_{\text{peak}}}^B} \quad (6)$$

421 where C and B indicate the COMP and BAND values respectively. This statistic has a  
 422 value of unity when the deviation between the  $E_{\text{peak}}$  values exactly matches the sum of the  
 423  $1\sigma$  errors. A value less than one indicates the  $E_{\text{peak}}$  values are within errors, and a value  
 424 greater than one indicates that the  $E_{\text{peak}}$  values are not within  $1\sigma$  errors of each other.  
 425 Figure 9 depicts the distribution of the statistic. Roughly 46% of the BAND and COMP  
 426  $E_{\text{peak}}$  values are found to be outside the combined errors. This indicates that, although  
 427 COMP is a special case of BAND, a significant fraction of the  $E_{\text{peak}}$  values can vary by more  
 428 than  $1\sigma$  based on which model is chosen. If the allowed error range is extended to  $3\sigma$  then  
 429 only 14% of the  $E_{\text{peak}}$  values are not consistent.

430 The distributions for the time-averaged energy flux and photon flux are shown in  
 431 Figure 10 and Figure 11, respectively. The photon and energy fluxes of the BEST sample  
 432 have a median value of around  $2.4 \text{ ph cm}^{-2} \text{ s}^{-1}$ , and  $3 \times 10^{-7} \text{ ergs cm}^{-2} \text{ s}^{-1}$ , respectively  
 433 in the 10-1000 keV band. When integrating over the full GBM spectral band, 10 keV -  
 434 40 MeV, the BEST energy flux distribution broadens significantly, approximating a top hat  
 435 function with a small high-flux tail spanning about 2 orders of magnitude. Note that the  
 436 low-flux cutoff is due to both the sensitivity of the instrument and the clear deviation from  
 437 a three-dimensional Euclidean distribution that is observed in a typical  $\log N$ - $\log S$  plot

438 (von Kienlin et al. submitted). In any case, the flux measurements with a more sensitive  
 439 instrument will likely position the peak of the flux distribution at a lower flux value (see  
 440 also Gruber et al. 2012). Similarly in Figure 12 and Figure 13, the distributions for the  
 441 BEST photon fluence and BEST energy fluence are depicted. The plots for the photon  
 442 fluence appear to contain evidence of the duration bimodality of GRBs. While there is  
 443 a discriminant peak at  $\sim 30$  photons  $\text{cm}^{-2}$  there is also a deviation from a log-normal  
 444 distribution at smaller photon fluence values. Fitting the photon fluence distribution in the  
 445 10-1000 keV band with a sum of two log-normal functions, we find peak values of  $31_{-23}^{+91}$  and  
 446  $1.1_{-0.6}^{+1.1}$  ph  $\text{cm}^{-2}$ , respectively. Similarly, the distribution of the energy fluence in the 10-1000  
 447 keV band can also be fit by the sum of two log-normal functions which result in peak values  
 448 of  $(3.2_{-2.5}^{+11.3}) \times 10^{-6}$  and  $(1.5_{-0.4}^{+0.6}) \times 10^{-7}$  erg  $\text{cm}^{-2}$ , respectively. It is interesting to note  
 449 that while the COMP model is largely unaffected by the change in energy band due to the  
 450 exponential cutoff, the PL model shifts to one order of magnitude higher energy fluence  
 451 values, as it overestimates the flux at higher energies (see Figure 12(d)). The brightest  
 452 GRB contained in this catalog based on time-averaged photon flux is GRB 120323.507  
 453 (Guiriec et al. 2013) with a flux of  $\sim 115$  ph  $\text{s}^{-1}$   $\text{cm}^{-2}$  and the burst with the largest  
 454 average energy flux is GRB 111222.619 with an energy flux of  $\sim 1.5 \times 10^{-5}$  ergs  $\text{s}^{-1}\text{cm}^{-2}$ .  
 455 The burst with the highest energy fluence is GRB 090902.462 (Abdo et al. 2009) with an  
 456 energy fluence of  $\sim 2.8 \times 10^{-4}$  ergs  $\text{cm}^{-2}$  while the burst with the highest photon fluence is  
 457 GRB 090618.353 with a photon fluence of  $> 2300$  ph  $\text{cm}^{-2}$ .

458 In Figure 14 we present the BEST rest-frame spectral parameters for  $E_{\text{peak}}$ ,  $E_{\text{b}}$ ,  $E_{\text{iso}}$   
 459 and  $L_{\text{iso}}$  where the latter two have been determined in the rest-frame energy band between  
 460  $1/(1+z)$  keV and  $10/(1+z)$  MeV. Both,  $E_{\text{peak}}^{\text{rest}}$  and  $E_{\text{break}}^{\text{rest}}$  peak at roughly 600 keV and,  
 461 similarly to the distributions in the observer frame, cover just two orders of magnitude. The  
 462  $E_{\text{iso}}$  distribution peaks at  $\sim 10^{53}$  erg and extends over more than three orders of magnitude.  
 463  $L_{\text{iso}}$ , on the other hand, has a median of  $\sim 10^{52}$  erg/s and covers 3 orders of magnitude.

464 In Figure 15 we show the evolution of the BEST spectral parameters,  $\alpha$ ,  $\beta$  and  $E_{\text{peak}}$ ,  
 465 with redshift. While both the high-energy index and  $E_{\text{peak}}$  do not show a clear dependence  
 466 with redshift (see also Gruber et al. 2011b), the low-energy index of the long GRBs shows  
 467 a trend to steeper, i.e. softer, values at higher redshifts (see also Geng & Huang 2013).  
 468 However, a Spearman rank correlation analysis shows that this correlation is not significant  
 469 ( $P = 0.15$ ).

### 470 6.1.1. The break scale $\Delta$

471 In order to test the behavior of the break scale  $\Delta$  of the SBPL model, we re-fitted all  
 472 GOOD SBPL spectra obtained from the  $F$  spectral fits. Contrary to the initial fits, we vary  
 473 the break scale, thus increasing the number of free model parameters. After the fit, we  
 474 applied the same quality cuts to the resulting parameters as for the GOOD SBPL sample  
 475 with the additional requirement that  $\sigma_{\Delta}/\Delta \leq 0.4$ . Out of the initial 384 SBPL fits only  
 476 36 fulfilled this newly added criterion, with the fit not able to constrain 5 free parameters  
 477 for the bulk of the GOOD sample. As intuitively obvious, only the most fluent portion of  
 478 the sample could be fitted with such a complex model (see Figure 16), but it should be  
 479 noted that the GRBs for which the break scale could be constrained are not necessarily the  
 480 GRBs for which this model was selected as BEST in Section 5.2. In Figure 17 we show the  
 481 distribution of  $\Delta$ . As can be seen  $\Delta$  varies between 0.1 and 0.7 with an average value of  
 482  $0.4 \pm 0.2$ . It is instructive to investigate how the additional free fit parameter affects the  
 483 results of the other model components. In Figure 18 we show the relations between fixed  
 484 and varying  $E_b$ , low- and high-energy power-law indices. The low-energy power-law index  
 485 seems to tend towards shallower values (particularly when the index is already shallow with  
 486 the fixed  $\Delta$ ) when letting  $\Delta$  vary freely. In fact, 13 (36%) low-energy power-law indices  
 487 are not consistent within  $1\sigma$ . The high-energy power-law index has a tendency to steepen

488 and 11 (31%) indices are not consistent within the  $1\sigma$  limit. With 8 (22%)  $1\sigma$  outliers, the  
 489 situation is similar for  $E_b$ . In general,  $E_b$  tends towards harder values when  $\Delta$  is allowed to  
 490 vary.

## 491 6.2. $P$ spectral fits

492 Similarly to the  $F$  spectral fits, we are going to present the results of the  $P$  spectral  
 493 fits in this section.

494 The  $P$  spectral distributions have been produced by fitting the GRB spectra over the  
 495 1024 ms and 64 ms peak flux duration of long and short bursts respectively. Note that  
 496 the results from both long and short bursts are included in the following figures. The  
 497 low-energy indices from the  $P$  selections of the BEST sample, as shown in Figure 19(b),  
 498 have a median value of about  $-1.3$  and show a bimodal distribution. This is due to the  
 499 fact that more GRBs of the  $P$  sample are best fit by the PL because, due to less photon  
 500 fluence accumulation, the signal-to-noise ratio decreases. 20% of the BEST low-energy  
 501 indices show  $\alpha > -2/3$  and violate the synchrotron “line-of-death”, while an additional  
 502 32% of the indices are  $\alpha < -3/2$  and violate the synchrotron cooling limit, both of which  
 503 are significantly larger percentages than those from the  $F$  spectra. The high-energy indices  
 504 in Figure 20 peak at about  $-2.2$  and again have a long tail toward steeper indices. The  
 505 number of unconstrained high-energy indices increases when compared to the  $F$  spectra,  
 506 again likely due to the poorer statistics resulting from shorter integration times. As has  
 507 been shown with the  $F$  spectral fits, the PL index serves as an average between low- and  
 508 high-energy indices for the BAND and SBPL functions.

509 Shown in Figure 21 is the  $\Delta S$  distribution for the  $P$  spectra. This distribution seems  
 510 consistent with the BATSE results found previously (Preece et al. 2002; Kaneko et al.

511 2006), but suffers from a deficit in values compared to the  $F$  fits largely due to the inability  
 512 of the data to sufficiently constrain the high-energy power law index. The distribution  
 513 peaks at  $\sim 1.3$  and has a median value of 1.64.

514 In Figure 22 and Figure 23, we show the distributions for  $E_b$  and  $E_{\text{peak}}$ , respectively.  
 515 As was evident from the  $F$  spectra, the  $E_b$  from the SBPL fits appears to peak at 100 keV.  
 516 The  $E_{\text{peak}}$  distribution for the BEST sample peaks around 260 keV and covers just over  
 517 two orders of magnitude, which is consistent with previous findings (Preece et al. 1998a;  
 518 Kaneko et al. 2006). It should be noted that the data over the short timescales in the  $P$   
 519 spectra do not often favor either the BAND or the SBPL model, resulting in large parameter  
 520 errors.

521 Even though it is less obvious, Figure 24 shows a correlation between the  $E_{\text{peak}}$  and  
 522 low-energy power-law index and its uncertainty which is similar to the  $F$  spectral fits.

523 In addition, we calculate and show the  $\Delta E_{\text{peak}}$  statistic in Figure 25 and, as was the  
 524 case with the  $F$  spectra,  $\sim 46\%$  of the BAND and COMP  $E_{\text{peak}}$  values are found to be outside  
 525 the combined errors. If the allowed error range is extended to  $3\sigma$  then only 8% of the  $E_{\text{peak}}$   
 526 values are not consistent.

527 The distributions for the peak energy flux and photon flux are shown in Figures 26 and  
 528 Figure 27, respectively. The photon flux of the BEST sample peaks around 4.5 photons  
 529  $\text{cm}^{-2} \text{s}^{-1}$ , and the energy flux of the BEST sample peaks at  $6.4 \times 10^{-7} \text{ ergs cm}^{-2} \text{s}^{-1}$  in the  
 530 10-1000 keV band. When integrating over the full GBM spectral band, 10 keV-40 MeV, the  
 531 dispersion in the energy flux increases and approximates a top hat function with a small  
 532 high-flux tail spanning about 2 orders of magnitude. The brightest short GRB in terms of  
 533 peak photon flux is GRB 120323.507 at  $> 580 \text{ ph s}^{-1} \text{ cm}^{-2}$  while the most energetic short  
 534 GRB is GRB 090227.772 with an energy flux of  $\sim 8.3 \times 10^{-5} \text{ ergs s}^{-1} \text{ cm}^{-2}$ .

535 In Figure 28 we present the rest-frame spectral parameters for  $E_{\text{peak}}$ ,  $E_{\text{b}}$ ,  $E_{\text{iso}}$  and  $L_{\text{iso}}$   
 536 of the  $P$  spectral fits where the latter two have been determined in the rest-frame energy  
 537 band between  $1/(1+z)$  keV and  $10/(1+z)$  MeV. Both,  $E_{\text{peak}}^{\text{rest}}$  and  $E_{\text{break}}^{\text{rest}}$  peak at roughly  
 538 600 keV and, similarly to the distributions in the observer frame, cover just two orders of  
 539 magnitude. The  $E_{\text{iso}}$  distribution is narrower than the one obtained from the  $F$  spectral fits  
 540 and has a median of  $\sim 10^{52}$  erg.  $L_{\text{iso}}$ , on the other hand, has a median of  $\sim 3 \times 10^{52}$  erg/s  
 541 and covers  $\sim 3$  orders of magnitude.

542 In Figure 29 we show the evolution of the BEST spectral parameters,  $\alpha$ ,  $\beta$  and  $E_{\text{peak}}$ ,  
 543 with redshift. None of the parameters shows a dependence with redshift.

### 544 6.3. Comparing the $F$ with the $P$ spectral fits

545 When studying the two types of spectra in this catalog, it is instructive to study the  
 546 similarities and differences between the resulting parameters. Plotted in Figure 30 are the  
 547 low-energy indices, high-energy indices, and  $E_{\text{peak}}$  energies of the  $P$  spectra as a function  
 548 of the corresponding parameters from the  $F$  spectra. Most of the  $P$  spectral parameters  
 549 correlate with the  $F$  spectral parameters on the order of unity. There are particular regions  
 550 in each plot where outliers exist, and these areas indicate that either the GRB spectrum  
 551 is poorly sampled or that significant spectral evolution exists in the  $F$  measurement of  
 552 the spectrum that skews the time-integrated spectral values. Examples of the former case  
 553 are when the low-energy index is  $\gtrsim -1.2$  or the high-energy index is steeper than average  
 554 ( $\lesssim -2$ ).

555 It is common belief that  $E_{\text{peak}}$  is significantly larger at the peak of the GRB, compared  
 556 to the average  $E_{\text{peak}}$ . Figure 30(c), and similar results found in Goldstein et al. (2012) and  
 557 Nava et al. (2011), seems to contradict this belief with marginal difference between  $E_{\text{peak}}$

558 measured at the peak of the photon flux and  $E_{\text{peak}}$  measured over the full duration of the  
559 burst.

560 However, time-resolved spectral analyses in the past have shown (e.g. Kaneko et al.  
561 2006; Lu et al. 2012, for BATSE and GBM GRBs, respectively) that two different  
562  $E_{\text{peak}}$ -evolution patterns can (co-)exist in a single GRB:

- 563 1.  $E_{\text{peak}}$  can evolve from hard-to-soft and/or
- 564 2.  $E_{\text{peak}}$  shows a tracking behavior with respect to the photon flux.

565 If a GRB evolves from hard-to-soft, the peak of the photon flux does not necessarily  
566 correspond to the highest  $E_{\text{peak}}$  value (see also Crider et al. 1999). Only when  $E_{\text{peak}}$  tracks  
567 the intensity its highest value is indeed expected at the peak photon flux.

568 In addition, the time-averaged  $E_{\text{peak}}$  is also dependent on the ratio of the peak photon  
569 flux versus the average photon flux of the GRB. A larger ratio, i.e. a higher photon flux  
570 at the peak of the burst, skews the average  $E_{\text{peak}}$  toward the  $E_{\text{peak}}$  found at peak flux.  
571 Therefore, a marginal difference between  $E_{\text{peak}}$  of the  $F$  spectral fits and  $P$  spectral is  
572 expected.

573 In a forthcoming catalog (Yu et al. in prep.), the results of a time-resolved study of  
574 GBM GRBs will be presented.

575 To aid in the study of the systematics of the parameter estimation, as well as the  
576 effect of statistics on the fitting process, we investigate the behavior parameter values as a  
577 function of accumulation time and the photon fluence for the  $F$  BEST spectra and peak  
578 photon flux for the  $P$  BEST spectra, respectively. These distributions are shown in Figures  
579 31, 32 and 33, respectively. As the photon fluence is correlated with the duration of a burst  
580 (see again Figure 1(b)) any correlation of a spectral parameter with the accumulation time

581 will also be correlated with photon fluence.

582 When fitting the time-integrated spectrum of a burst, we find the low- and high-energy  
 583 indices trend towards steeper values for bursts with longer accumulation times. The  
 584 simple PL index trends from shallow values of  $\sim -1.3$  to a steeper value of  $\sim -2$ . The  
 585 low-energy index for a spectrum with curvature tends to exhibit an unusually shallow value  
 586 of  $\sim -0.4$  for short GRBs or extremely low fluence spectra, and steepens to  $\sim -1.5$  for  
 587 longer GRBs or higher fluence spectra. Similarly, the high-energy index trends from  $\sim -1.2$   
 588 at short durations or low fluence to  $\sim -2.7$  at long durations or high fluence, although  
 589 this is complicated by unusually steep and poorly constrained indices that indicate that an  
 590 exponential cutoff may result in a more reliable spectral fit. When inspecting the  $E_{\text{peak}}$  as  
 591 a function of accumulation time the resulting plot is reminiscent of the hardness/duration  
 592 correlation with two distinct regions for the long and short GRBs. As for the correlation  
 593 between  $E_{\text{peak}}$  and photon fluence a trend is much less apparent. If a burst is assumed to  
 594 have significant spectral evolution, then obviously the  $E_{\text{peak}}$  will change values through the  
 595 time history of the burst, typically following the traditional hard-to-soft energy evolution.  
 596 For this reason, spectra that integrate over increasingly more time will tend to suppress the  
 597 highest energy of  $E_{\text{peak}}$  within the burst, so a general decrease in  $E_{\text{peak}}$  is expected with  
 598 longer integration times. However, the photon fluence convolves the integration time with  
 599 the photon flux. This means that an intense burst with a short duration and high  $E_{\text{peak}}$  may  
 600 have on the order the same fluence as a much longer but less intense burst with a smaller  
 601  $E_{\text{peak}}$ . This causes significant broadening to the decreasing trend as shown in Figure 32(c).

602 The distribution of parameters as a function of the peak photon flux, however, is much  
 603 less clear. The distributions shown in Figure 33 are more susceptible to uncertainty because  
 604 of smaller statistics involved in the study of the  $P$  section of the GRB, except in some cases  
 605 where the peak photon flux is on the order of the photon fluence. Ignoring the regions where

606 the parameters are poorly constrained, another trend emerges from the low-energy indices;  
 607 they appear to become slightly more shallow as the photon flux increases. The high-energy  
 608 indices, however, appear to be unaffected by the photon flux, although a trend of steeper  
 609 indices with higher photon fluxes seems apparent. Finally, no obvious trend is visible for  
 610  $E_{\text{peak}}$  as a function of the peak photon flux (Spearman rank correlation coefficient of -0.05  
 611 with a chance probability of  $P = 0.9$ ). However, when inspecting  $E_{\text{peak}}$  as a function of  
 612 peak energy flux a correlation becomes apparent (Spearman rank correlation coefficient of  
 613 of  $\sim 1$  with  $P = 8 \times 10^{-08}$ ). The lack and existence of a correlation between  $E_{\text{peak}}$  and  
 614 the photon and energy flux, respectively is expected because it is the energy of collected  
 615 photons and not their number that drives the hardness (and thus  $E_{\text{peak}}$ ) of a GRB.

616 The spectral results, including the best fit spectral parameters and the photon model,  
 617 are stored in files following the FITS standard and will be hosted as a public data archive  
 618 on HEASARC<sup>3</sup>. The values returned by default in a Browse search of the catalog are the  
 619 most recent values, which will be the results presented here upon acceptance of this paper.  
 620 However, the values and results obtained by Goldstein et al. (2012) will still be available by  
 621 ftp. The keyword *scatalog* indicates which catalog a file belongs to. Both the differences  
 622 between the methodologies and how to retrieve the older files will be fully documented at  
 623 HEASARC.

## 624 7. Summary & Discussion

625 After four successful years, GBM continues to be a prime instrument for GRB  
 626 observations. The second GBM spectral catalog includes 943 GRBs detected by GBM  
 627 during 4 years of operation. We presented the spectral properties of these bursts both from

---

<sup>3</sup><http://heasarc.gsfc.nasa.gov/W3Browse/fermi/fermigbrst.html>

628 a time-integrated, and a peak flux analysis. Four photon model fits were applied to each  
 629 selection, resulting in more than 7500 spectral fits. We have described subsets of the full  
 630 results in the form of data cuts based on parameter uncertainty, as well as employing model  
 631 comparison techniques to select the most statistically preferred model for each GRB. The  
 632 analysis of each GRB was performed as objectively as possible, in an attempt to minimize  
 633 biased systematic errors inherent in subjective analysis. The methods we have described  
 634 treat all bursts equally, and we have presented the ensemble of observed spectral properties  
 635 of GBM GRBs.

636 Although most of the resulting parameter distributions are similar to the ones found by  
 637 other GRB missions, some contain important differences. For example, thanks to the two  
 638 BGO detectors, burst data extend into the high-energy domain which, in the past, has been  
 639 accessible only by the *Solar Maximum Mission* Gamma Ray Spectrometer (Harris & Share  
 640 1998) and the PHEBUS instrument onboard the Granat spacecraft (Barat et al. 1993).  
 641 While there does not seem to be a new population of bursts with high  $E_{\text{peak}}$  values in  
 642 their time-integrated spectra, 40 GRBs of the BEST fluence spectra and 37 of the BEST  
 643  $P$  spectrum have  $E_{\text{peak}}$  values above 1 MeV. In order to verify whether the lack of GRBs  
 644 with high  $E_{\text{peak}}$  values in their time-integrated spectra is intrinsic or an instrumental bias  
 645 (decreasing effective area in the BGOs) requires simulations which go beyond the scope of  
 646 this catalog. We emphasize that there are indeed GRBs with very high  $E_{\text{peak}}$  values in  
 647 their time-resolved spectra, such as e.g. GRB 110721A (Axelsson et al. 2012) which has the  
 648 highest observer-frame  $E_{\text{peak}}$  value ( $15 \pm 2$  MeV) known to date. In a forthcoming catalog  
 649 of time-resolved spectra of GBM GRBs (Yu et al. in prep.) this will be investigated in more  
 650 detail.

651 Another interesting result of the parameter distributions is the  $\Delta S$  parameter, the  
 652 difference between the low- and high-energy spectral indices. This is an important quantity

653 because current models for the GRB prompt emission mechanism can be broken into  
 654 two categories: magnetic (e.g. Lee et al. 2000) or driven by internal/external shocks (e.g.  
 655 Rees & Meszaros 1992). Thus, by comparing  $\Delta S$  to the predictions by the synchrotron  
 656 shock model, it is possible to obtain useful insights into the emission mechanisms of GRBs.  
 657 As our results for the  $\Delta S$  distribution are compatible and in line with the results obtained  
 658 by Preece et al. (2002) and Kaneko et al. (2006) it can be concluded that the predictions of  
 659 the SSM model, in its simplest form, are not reconcilable neither with the observations  
 660 made by BATSE nor those performed by GBM.

661 Thanks to the rapid localizations of the *Swift* satellite, necessary to identify a redshift  
 662 for any given burst, and the broad coverage of the GBM we could study many spectral  
 663 properties in the rest-frame of the GRB. This results in the largest  $E_{\text{peak}}^{\text{rest}}$ ,  $E_{\text{iso}}$  and  $L_{\text{iso}}$   
 664 sample to date which have been analyzed coherently and consistently with an unified  
 665 methodology, thus minimizing systematic effects. This may be helpful in assessing whether  
 666 or not well known correlations in the GRB literature are indeed real or due to statistical  
 667 fluctuations and systematical issues.

668 The differences between various GBM spectral catalogs (e.g. Nava et al. 2011) were  
 669 extensively discussed in Goldstein et al. (2012). Small discrepancies between Goldstein et al.  
 670 (2012)’s first GBM spectral catalog and the one presented here (e.g. different BEST  
 671 models for the same GRB, fraction of bursts best fit with a given model) are mainly due  
 672 to enhanced and modified criteria in determining the BEST and GOOD sample, updated  
 673 analysis software and response matrices and the usage of different statistical criteria, i.e.  
 674 C-Stat instead of  $\chi^2$  to determine the preferred model. These differences are representative  
 675 of divergent methodologies and samples; therefore the reader should take care to understand  
 676 how the values in the catalogs are derived. Certainly, there are avenues of investigation  
 677 that require more detailed work and analysis or perhaps a different methodology. This

678 catalog should be treated as a starting point for future research on interesting bursts and  
679 ideas. As has been the case in previous GRB spectral catalogs, we hope this catalog will be  
680 of great assistance and importance to the search for the physical properties of GRBs and  
681 other related studies.

682

## 8. Acknowledgments

683 We thank the reviewer for his/her comments, which significantly contributed to  
684 improving the quality of the publication. The GBM project is supported by the German  
685 Bundesministeriums für Wirtschaft und Technologie (BMWi) via the Deutsches Zentrum  
686 für Luft und Raumfahrt (DLR) under the contract numbers 50 QV 0301 and 50 OG 0502.

## REFERENCES

687

688 Ade, P. A. R., Aghanim, N., Armitage-Caplan, C. et al. 2013, arXiv: 1303.50761

689 Abdo, A. A., Ackermann, M., Ajello, M. et al. 2009, ApJ, 706, 138

690 Ackermann, M., Asano, K., Atwood, W. B., et al. 2010, ApJ, 716, 1178

691 Ackermann, M., Ajello, M., Asano, K., et al. 2011, ApJ, 729, 114

692 Ackermann, M., Ajello, M., Allafort, A., et al. 2012, ApJ, 745, 144

693 Ackermann, M., Ajello, M., Baldini, L., et al. 2012, ApJ, 754, 121

694 Axelsson, M., Baldini, L., Barbiellini, G., et al. 2012, ApJ, 757, 31

695 Atwood, W. B., Abdo, A. A., Ackermann, M., et al. 2009, ApJ, 697, 1071

696 Band, D. L., Matteson, J., Ford, L., et al. 1993, ApJ, 413, 281

697 Barat, C., Skinner, G. K., & Lestrade, J. P. 2006, AdSpR, 38, 1329

698 Bissaldi, E., von Kienlin, A., Lichti G., et al. 2009, *Exp. Astron.*, 24, 47

699 Briggs, M. S., Band, D. L., Kippen R. M., et al. 1999, ApJ, 524, 82

700 Briggs, M. S., et al. 2013, J. Geophys. Res. Space Physics, 50205

701 Case, G. L., Cherry, M. L., Wilson-Hodge C. A., et al. 2011, ApJ, 729, 105

702 Cash, W. 1979, ApJ, 228, 939

703 Collazzi, A. C., et al. 2011, ApJ, 729, 89

704 Crider, A. C., Liang, E. P., Preece, R. D., et al. 1999, ApJ, 519, 206

705 Geng, J. J. & Huang, Y. F., 2013, ApJ, 764, 75

- 706 Ghirlanda, G., Ghisellini, G., & Lazzati, D. 2004, *ApJ*, 616, 331
- 707 Goldstein, A., Burgess, J. M., Preece, R. D., et al. 2012, *ApJS*, 199, 19
- 708 Gruber, D., Lachowicz, P., Bissaldi, E., et al. 2011, *A&A*, 533, 61
- 709 Gruber, D., Greiner, J., von Kienlin, A., et al. 2011, *A&A*, 531, 20
- 710 Gruber, D., et al. 2012, *PoS*, GRB 2012, 036
- 711 Guiriec, S., Briggs, M. S., Connaughton, V., et al. 2010, *ApJ*, 725, 225
- 712 Guiriec, S., Connaughton, V., Briggs, M. S., et al. 2011, *ApJ*, 727, 33
- 713 Guiriec, S., Daigne, F., Hascoët, R., et al. 2013, *ApJ*, 770, 32
- 714 Harmon, B. A., Fishman, G. J., Wilson, C. A., et al. 2002, *ApJS*, 138, 149
- 715 Harris, M. J. & Share, G. H. 1998, *ApJ*, 494, 724
- 716 Hoover, A. S., et al. 2008, *AIP Conf. Proc.* 1000, *Gamma-Ray Bursts 2007: Proceedings of*  
717 *the Santa Fe Conference*, ed. M. Galassi, D. Palmer, & E. Fenimore, 565
- 718 Hoover, A., Kippen, M., & Wallace, M. 2010, *General Response Simulation System*  
719 *(GRESS) Software User’s Guide*, Document GRESS-SUG-001-21 (Los Alamos, NM:  
720 LANL), <http://public.lanl.gov/mkippen/gress/>
- 721 Israel, G. L., Romano, P., Mangano, V., et al. 2008, *ApJ*, 685, 2
- 722 Kaneko, Y., Preece, R. D., Briggs, M. S., et al. 2006, *ApJS*, 166, 298
- 723 Kouveliotou, C., Meegan, C. A., Fishman, G. J., et al. 1993, *ApJ*, 413, L101
- 724 Lebrun, F., Leray, J. P., Lavocat, P., et al. 2003, *A&A*, 411, L141
- 725 Lee, H. K., Wijers, R. A. M. J., & Brown, G. E. 2000, *Phys. Rep.*, 325, 83

- 726 Lin, L., Kouveliotou, C., Baring, M. G., et al. 2011, *ApJ*, 739, 87
- 727 Lloyd, N. M., Petrosian, V., & Mallozzi, R. S. 2000, *ApJ*, 534, 227
- 728 Lu, R.-J., Wei, J.-J., Liang, E.-W., et al. 2012, *ApJ*, 756, 112
- 729 Mallozzi, R. S., Paciesas, W. S., Pendleton, G. N., Briggs, M. S., Preece, R. D., Meegan,  
730 C. A., & Fishman, G. J. 1995, *ApJ*, 454, 597
- 731 Meegan, C. A., Lichti, G., Bhat, P. N., et al. 2009, *ApJ*, 702, 791
- 732 Mitrofanov, I. G., Anfimov, D. S., Litvak, M. L., et al. 1999, *ApJ*, 522, 1069
- 733 Nava, L., Ghirlanda, G., Ghisellini, G., & Celotti, A. 2011, *A&A*, 530, A21
- 734 Paciesas, W. S., Meegan, C. A., von Kienlin, A., et al. 2012, *ApJS*, 199, 18
- 735 Planck Collaboration. 2005, ESA publication ESA-SCI(2005)/01, arXiv:astro-ph/0604069
- 736 Preece, R. D., Pendleton, G. N., Briggs, M. S., et al. 1998, *ApJ*, 496, 849
- 737 Preece, R. D., Briggs, M. S., Mallozzi, R. S., et al. 1998, *ApJ*, 506, 23
- 738 Preece, R. D., Briggs, M. S., Giblin, T. W., et al. 2002, *ApJ*, 581, 1248
- 739 Rees, M. J. & Meszaros, P. 1992, *MNRAS*, 258, 41P
- 740 Ryde, F., 1999, *Astro. Lett. and Comm.*, 39, 281
- 741 Sari, R., Piran, T., & Narayan, R. 1998, *ApJ*, 497, L17
- 742 Szécsi, D., Bagoly, Z., Kóbori, J. et al. 2013, *A&A*, 557, 8
- 743 Vedrenne, G., Roques, J.-P., Schönfelder, V., et al. 2003, *A&A*, 411, L63

- 744 von Kienlin, A., Briggs, M. S., Connoughton, V., et al. 2009, AIP Conf. Proc. 1133,  
745       Gamma-ray Bursts: Sixth Huntsville Symposium, ed. C. A. Meegan, C. Kouveliotou,  
746       & N. Gehrels, 446
- 747 von Kienlin, A., Gruber, D., Kouveliotou, C., et al. 2012, ApJ, 755, 150
- 748 von Kienlin, A., Meegan, C. A., Paciesas, W. S., et al. 2013, ApJS, submitted
- 749 Yu, H. F. , et al. in preparation

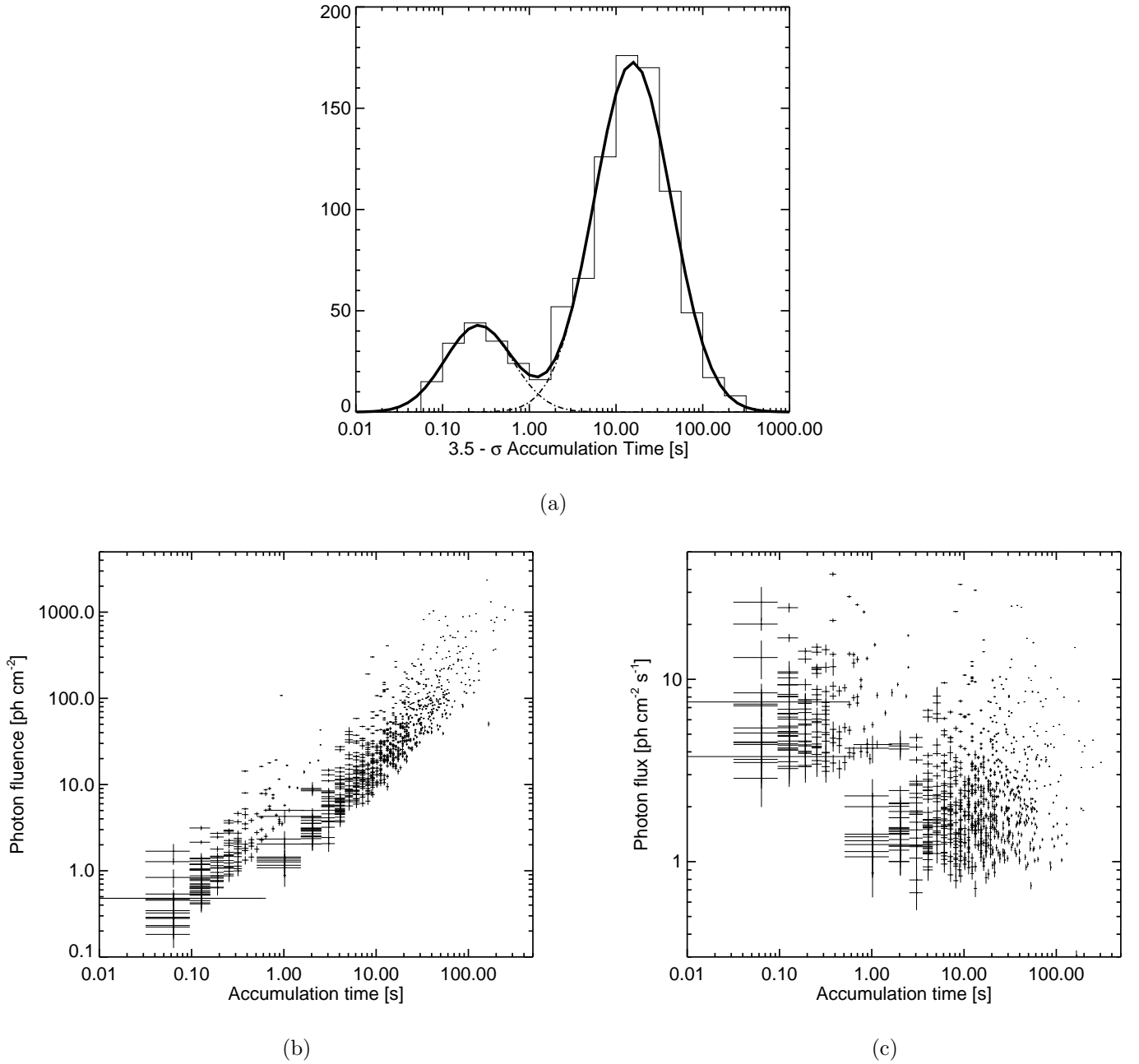


Fig. 1.— (a) is the distribution of the accumulation times based on the  $3.5\sigma$  signal-to-noise selections. Note the similarity to the traditional  $t_{90}$  distribution, with the minimum near 1 second. No other estimation of the duration was factored into the production of the accumulation time. (b) and (c) show the comparison of the model photon fluence and model photon flux to the accumulation time respectively. The photon fluences and fluxes shown in these figures are from the estimated BEST model fits.

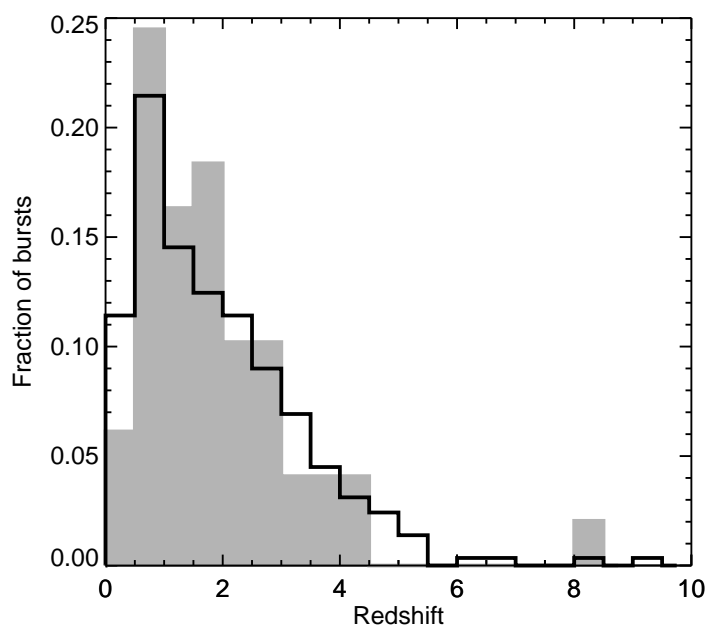
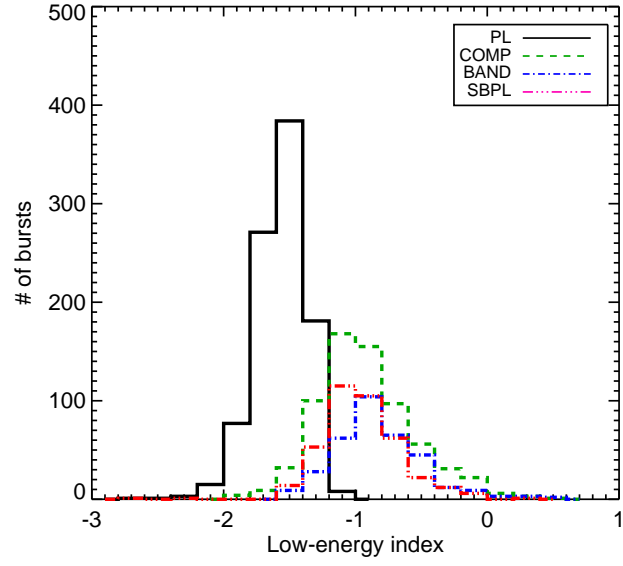
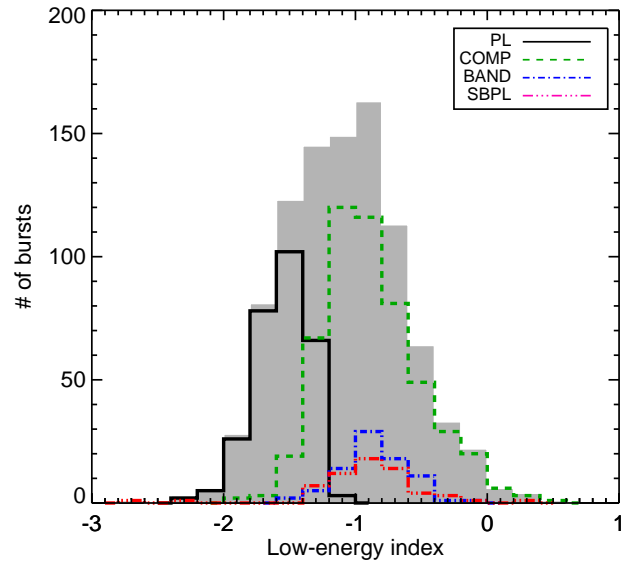


Fig. 2.— Redshift distribution of all GRBs with known redshift to date (black histogram) and GBM GRBs with known redshift (gray filled histogram) normalized to the area.

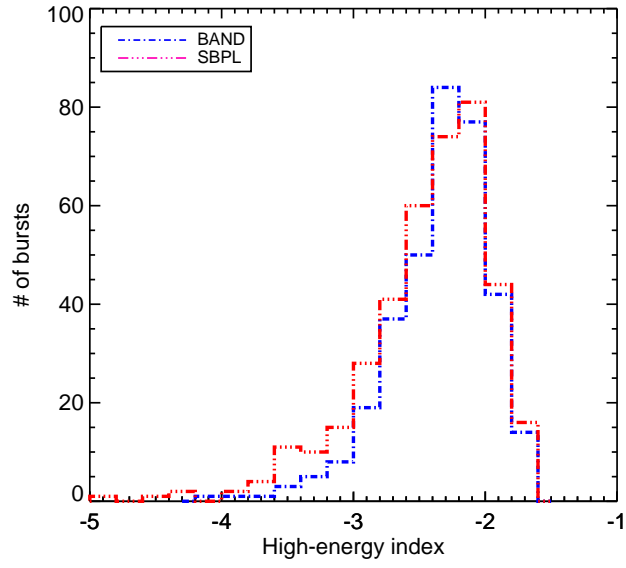


(a)

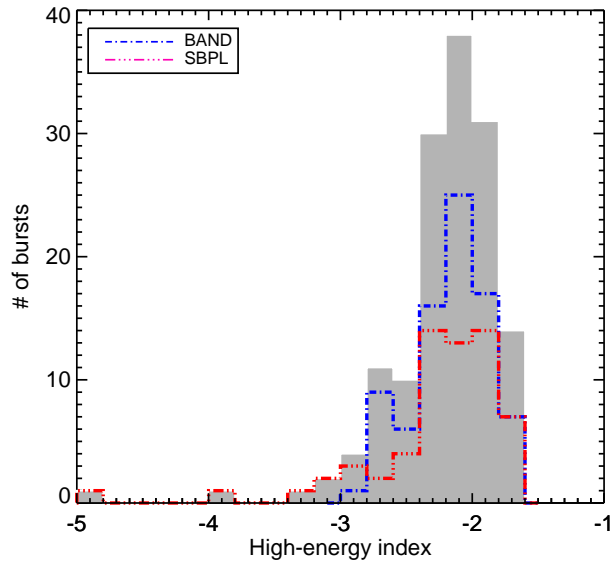


(b)

Fig. 3.— Distribution of the low-energy indices obtained from the GOOD  $F$  spectral fits (a). The BEST parameter distribution (gray filled histogram) and its constituents for the low-energy index is shown in (b).

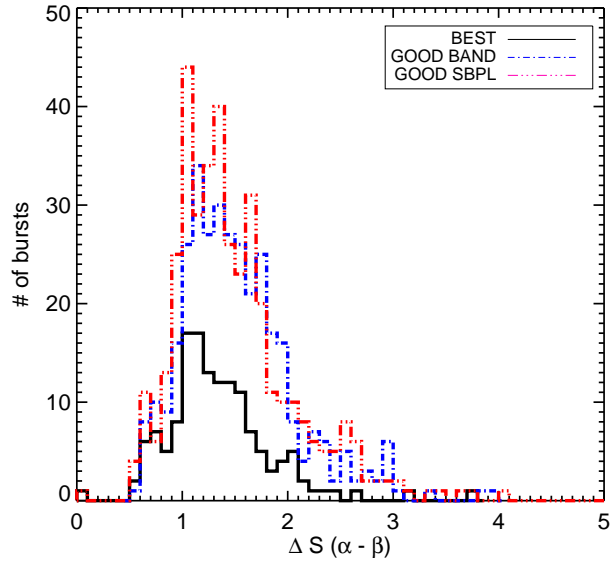


(a)



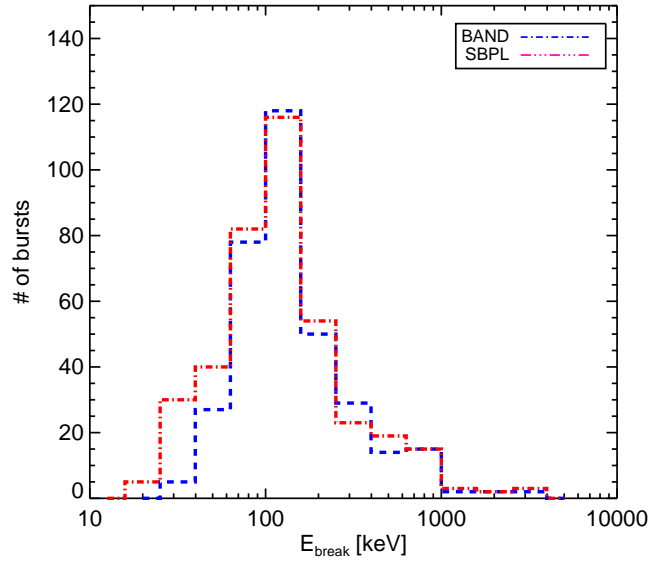
(b)

Fig. 4.— Distribution of the high-energy indices obtained from the GOOD  $F$  spectral fits (a). The BEST parameter distribution (gray filled histogram) and its constituents for the high-energy index is shown in (b).

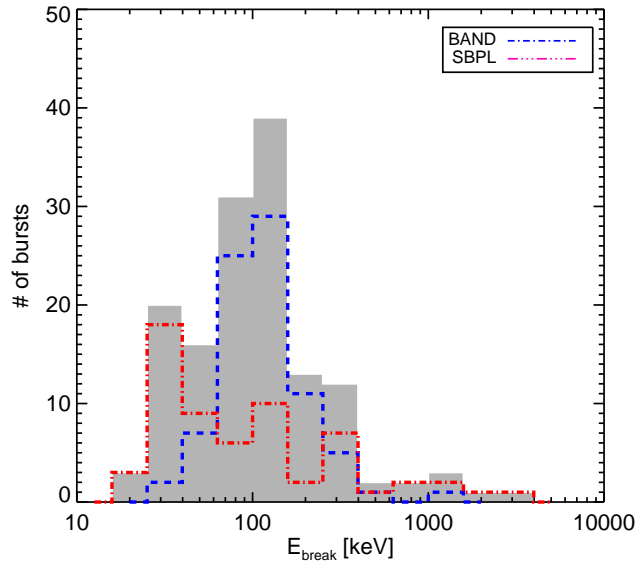


(a)

Fig. 5.— Distributions of  $\Delta S$ , the difference between the low- and high-energy spectral indices ( $\alpha - \beta$ ) for the  $F$  spectral fits. The BEST (black solid line), the GOOD BAND power-law indices (blue dash-dotted line) and the GOOD SBPL power-law indices (red dash-dot-dot-dotted line) for the  $F$  spectral fits are shown. The first bin contains values less than 0, indicating that the centroid value of  $\alpha$  is steeper than the centroid value of  $\beta$ .

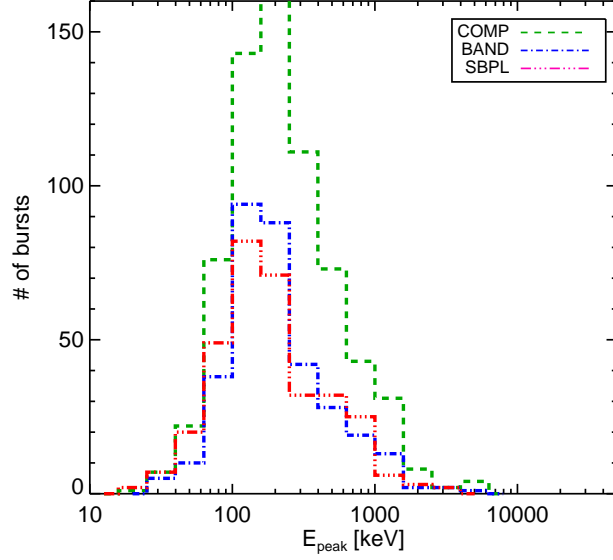


(a)

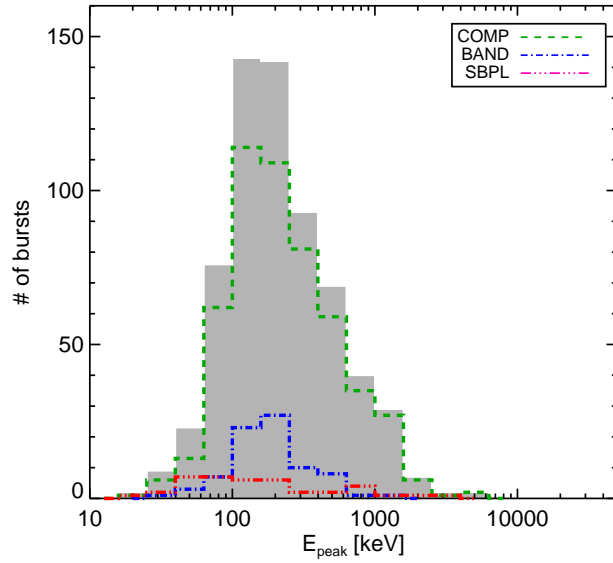


(b)

Fig. 6.— Distribution of the  $E_b$  obtained from the GOOD  $F$  spectral fits (a). The BEST parameter distribution (gray histogram) and its constituents for  $E_b$  is shown in (b). The  $E_b$  of the BAND model fits has been derived following Kaneko et al. (2006).

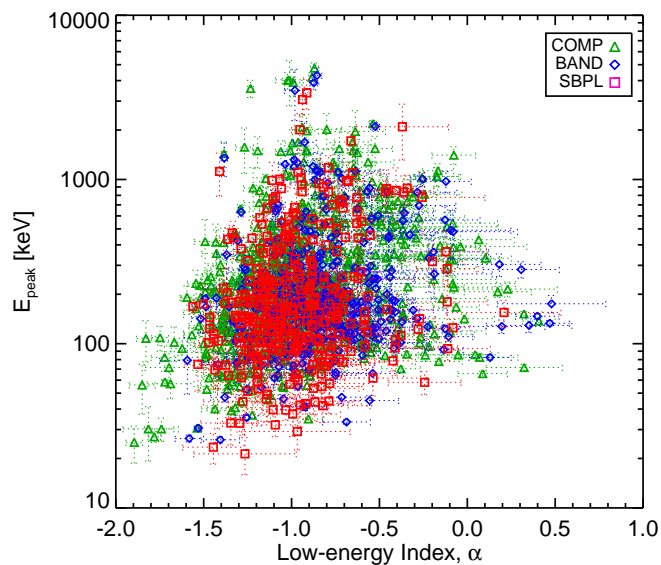


(a)

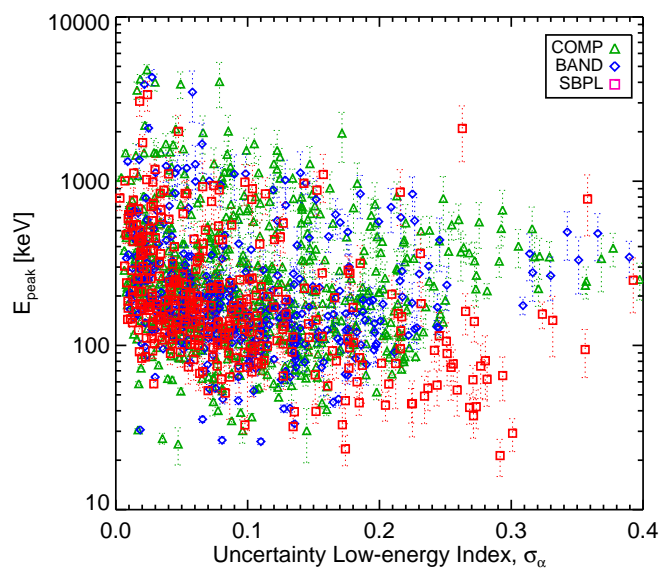


(b)

Fig. 7.— Distribution of the  $E_{\text{peak}}$  obtained from the GOOD  $F$  spectral fits (a). The BEST parameter distribution (gray filled histogram) and its constituents for  $E_{\text{peak}}$  is shown in (b).

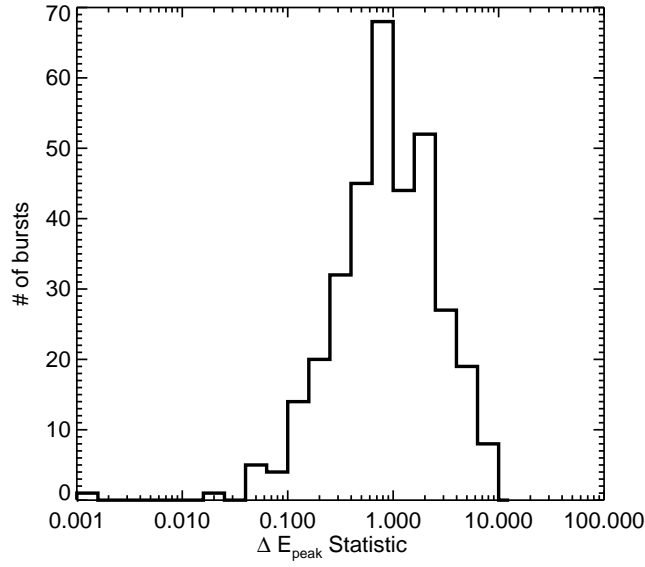


(a)



(b)

Fig. 8.— Comparison of the low-energy index and  $E_{\text{peak}}$  for three models from the  $F$  spectral fits. This comparison reveals a correlation between (a) the  $E_{\text{peak}}$  energy and the low-energy power-law index and (b) the  $E_{\text{peak}}$  and the uncertainty on the low-energy index. Generally a lower energy  $E_{\text{peak}}$  tends to result in a softer and a less constrained low-energy index.



(a)

Fig. 9.— Distribution of the  $\Delta E_{\text{peak}}$  statistic for the GOOD COMP and BAND models from  $F$  spectral fits. A value less than 1 indicates the  $E_{\text{peak}}$  values are within errors, while a value larger than 1 indicates the  $E_{\text{peak}}$  values are not within errors.

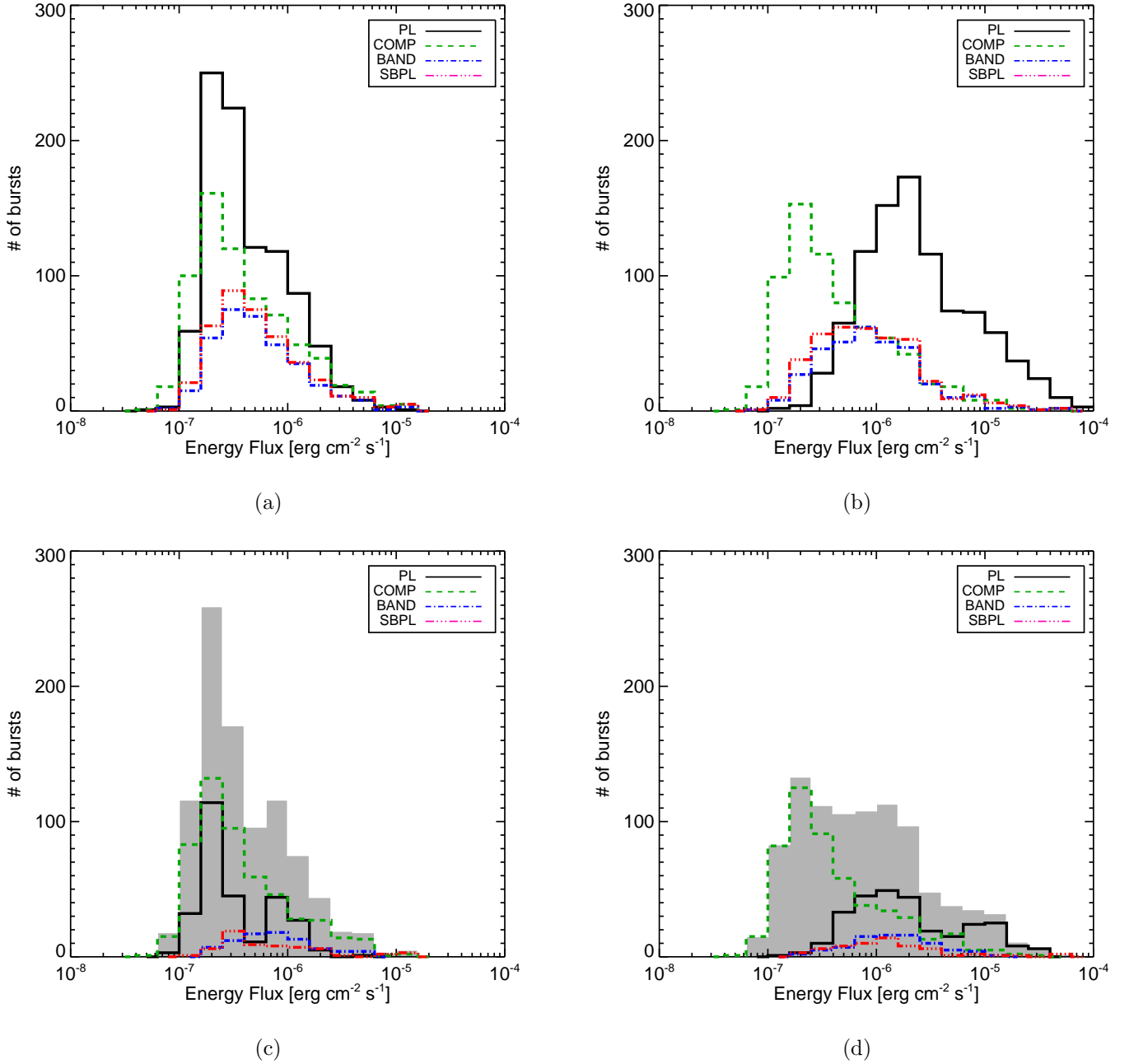


Fig. 10.— Distributions of energy flux in the 10 keV–1 MeV (a) and 10 keV–40 MeV (b) band from the GOOD  $F$  spectral fits. Note that the plotted distributions contain the flux on two different timescales: 1024 ms (long GRBs) and 64 ms (short GRBs). The BEST parameter distribution for the energy flux in both energy ranges is shown in (c) and (d). The gray filled histogram shows the total distribution and the constituents are shown in colors.

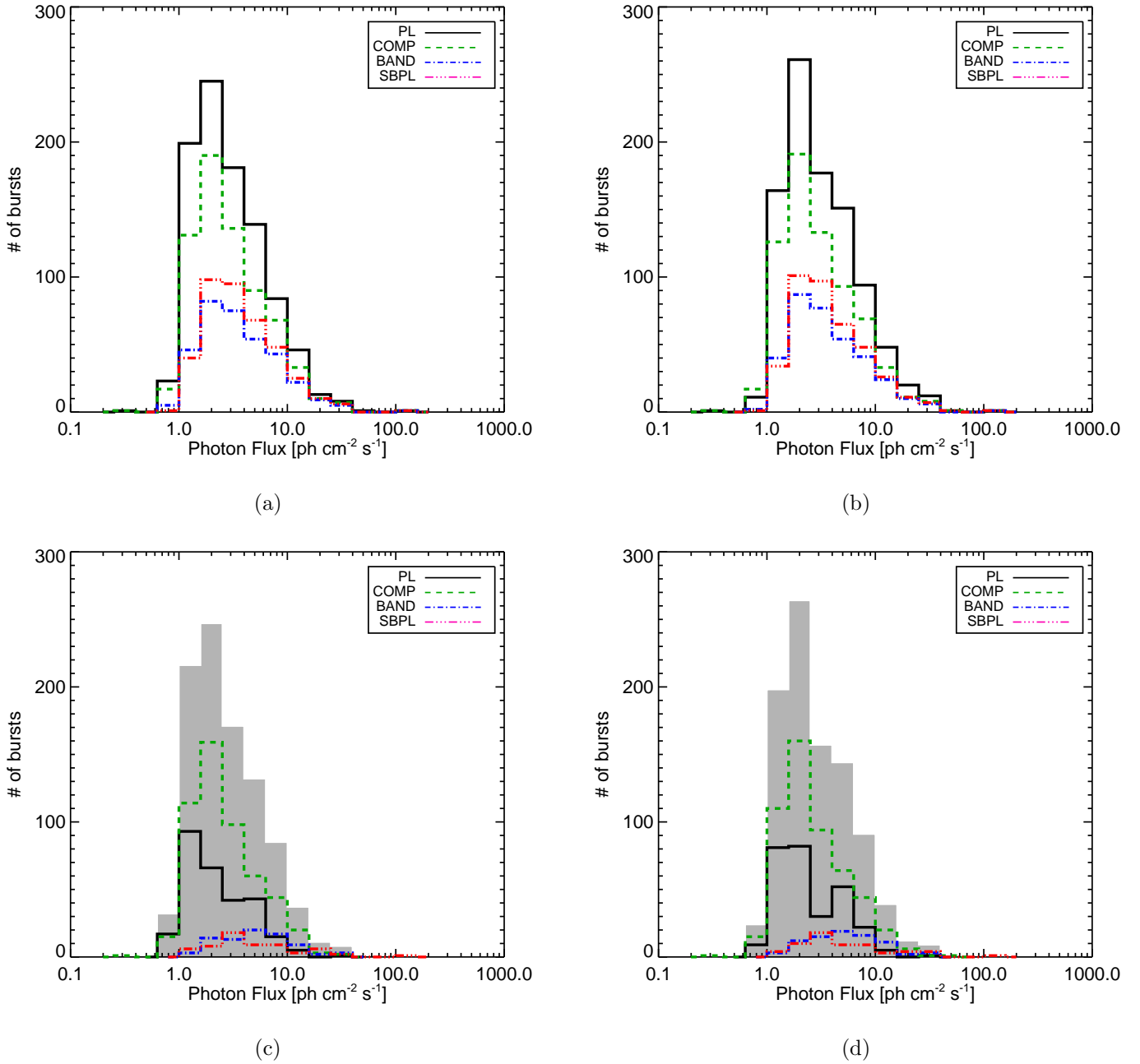


Fig. 11.— Distributions of photon flux in the 10 keV–1 MeV (a) and 10 keV–40 MeV (b) band from the GOOD  $F$  spectral fits. Note that the plotted distributions contain the flux on two different timescales: 1024 ms (long GRBs) and 64 ms (short GRBs). The BEST parameter distribution for the photon flux in both energy ranges is shown in (c) and (d). The gray filled histogram shows the total distribution and the constituents are shown in colors.

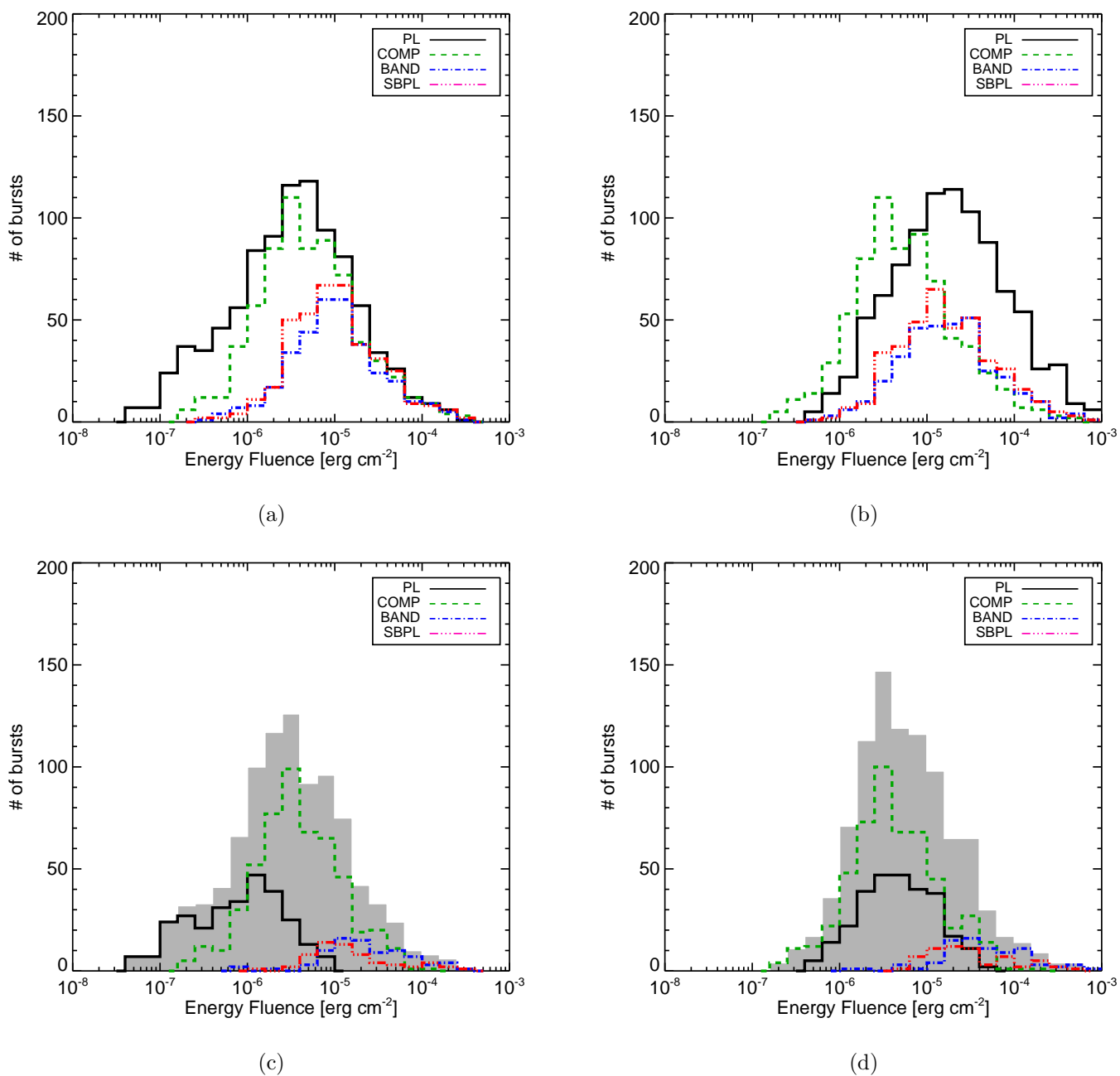


Fig. 12.— Distributions of energy fluence in the 10 keV–1 MeV (a) and 10 keV–40 MeV (b) band from the GOOD  $F$  spectral fits. The BEST parameter distribution for the energy fluence in both energy ranges is shown in (c) and (d). The gray filled histogram shows the total distribution and the constituents are shown in colors.

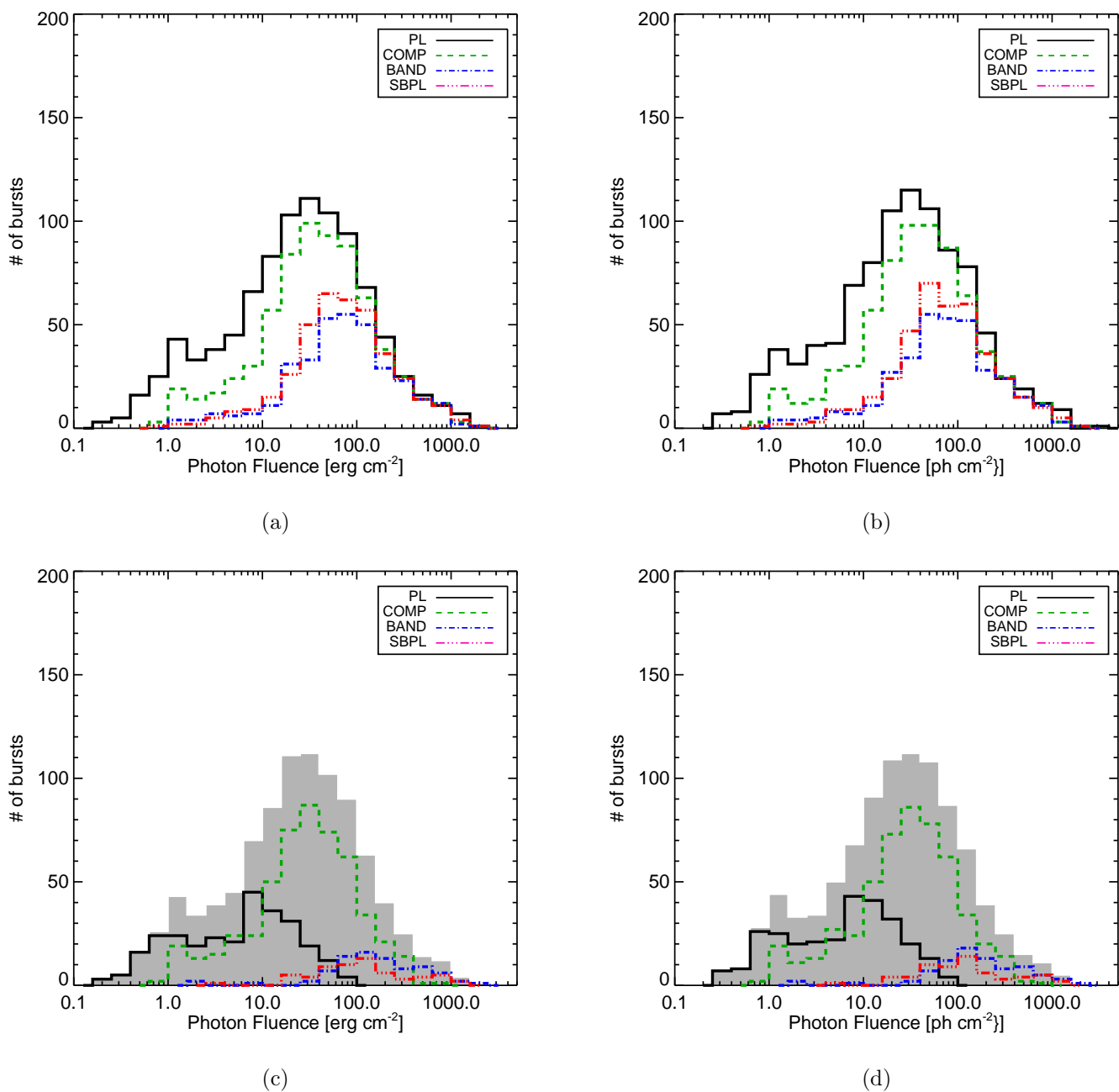


Fig. 13.— Distributions of photon fluence in the 10 keV–1 MeV (a) and 10 keV–40 MeV (b) band from the GOOD  $F$  spectral fits. The BEST parameter distribution for the energy fluence in both energy ranges is shown in (c) and (d). The gray filled histogram shows the total distribution and the constituents are shown in colors.

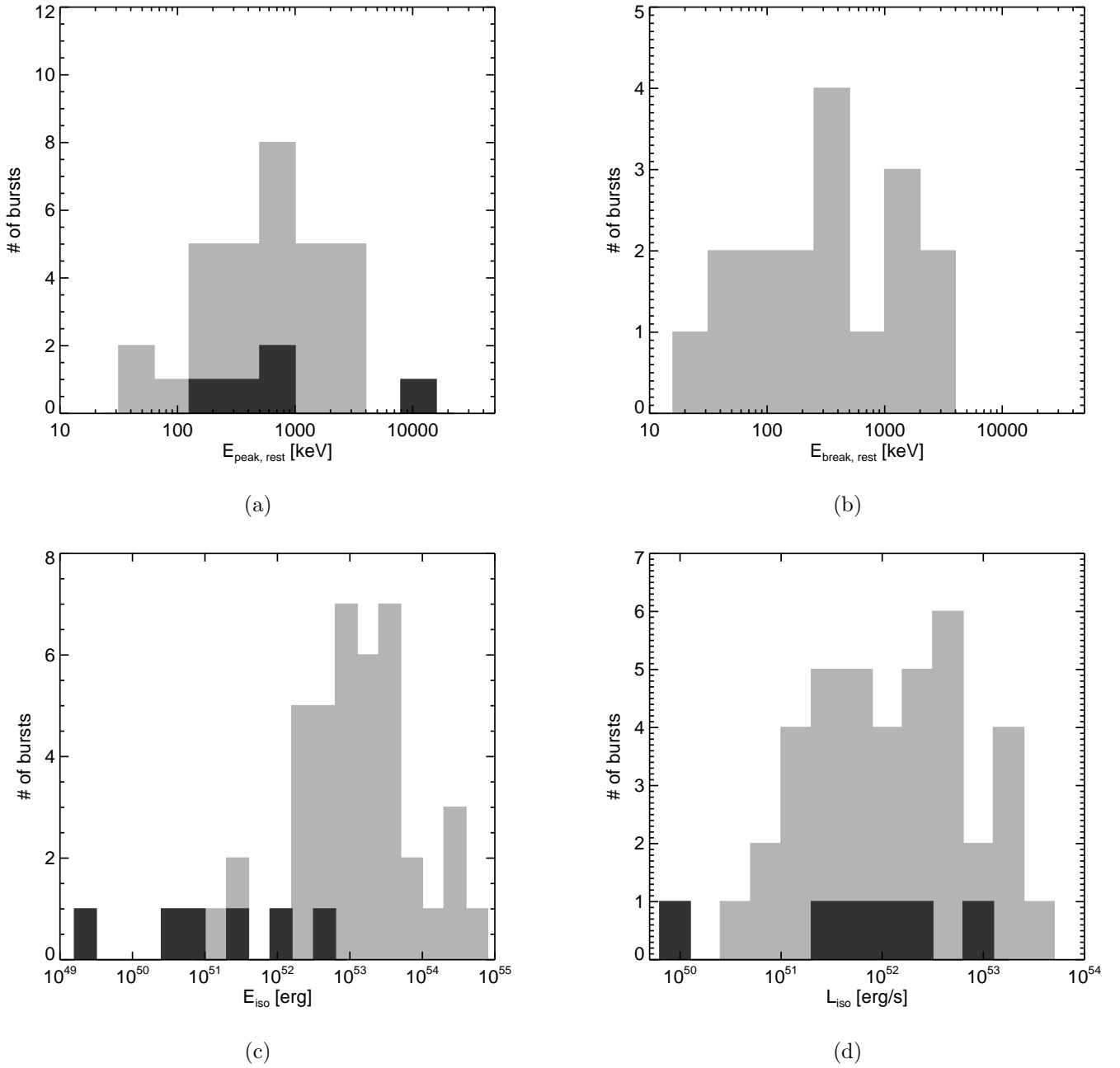


Fig. 14.— (a)  $E_{\text{peak}}^{\text{rest}}$  distribution of the  $F$  spectra fits from the BEST sample for long and short GRBs (light gray and dark gray filled histogram, respectively). (b) Same as (a) but for  $E_{\text{break}}^{\text{rest}}$ . (c) and (d) Distribution of  $E_{\text{iso}}$  and  $L_{\text{iso}}$  of the fluence spectral fits from the BEST sample in the rest-frame energy band  $1/(1+z)$  keV to  $10/(1+z)$  MeV.

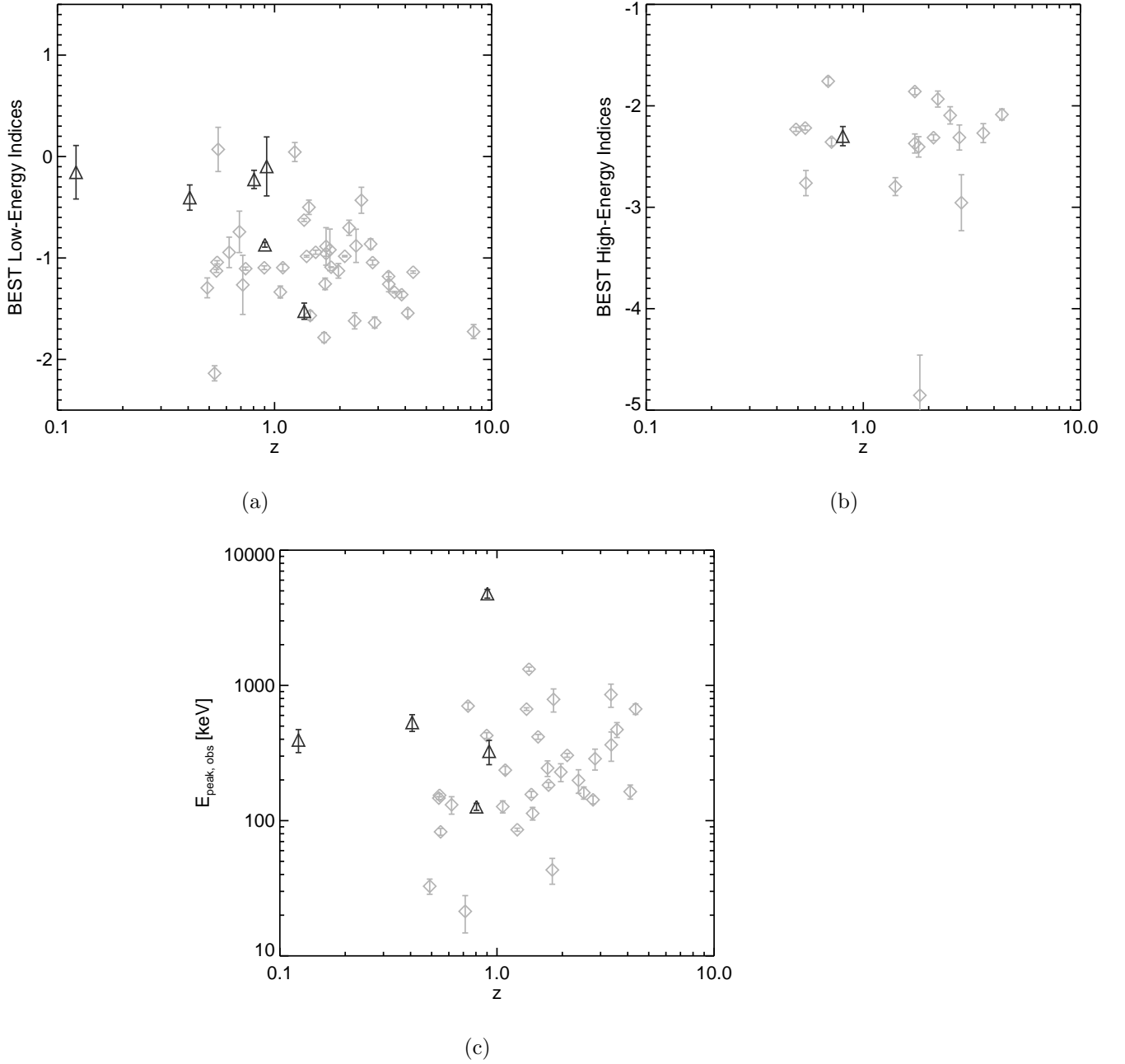
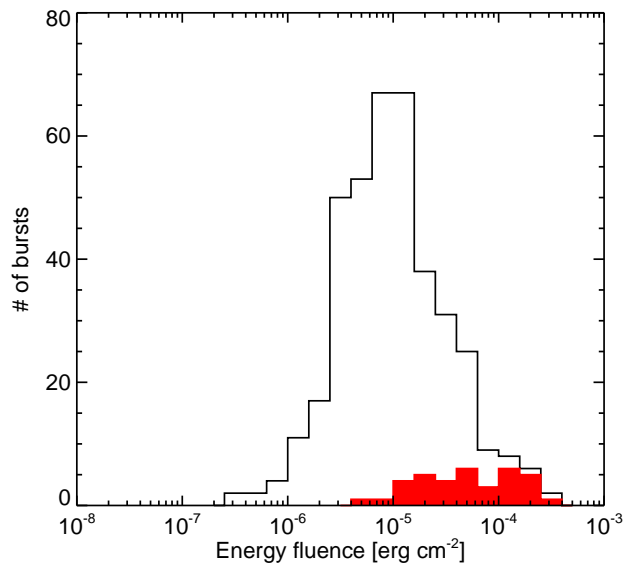
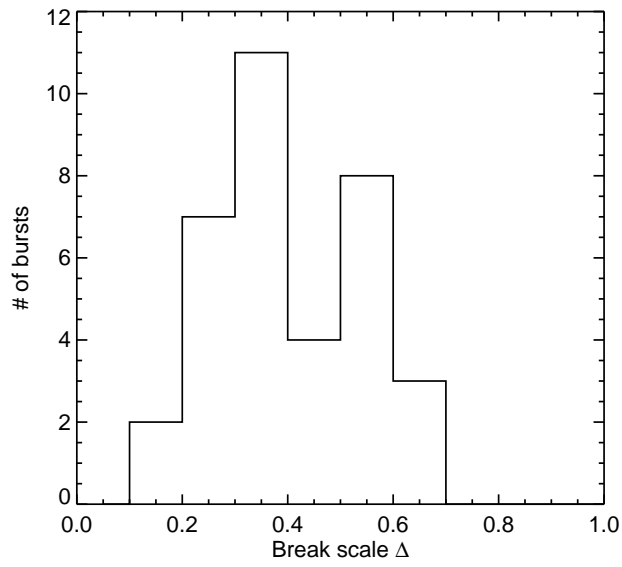


Fig. 15.— BEST spectral parameters as a function of the redshift of the  $F$  spectral fits for short (black triangles) and long (light-gray diamonds) GRBs.



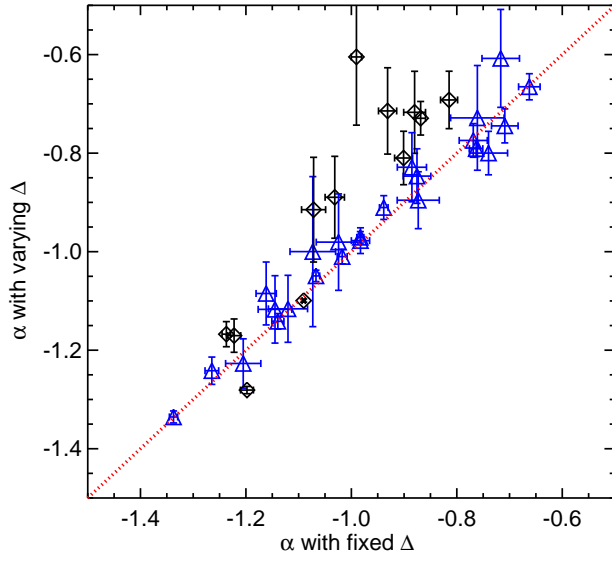
(a)

Fig. 16.— Distribution of the energy fluence in the 10 keV–1 MeV energy range for the GOOD SBPL  $F$  spectral fits (black solid histogram) and the GOOD SBPL fluence spectral fits with varying break scale  $\Delta$  (red filled histogram).

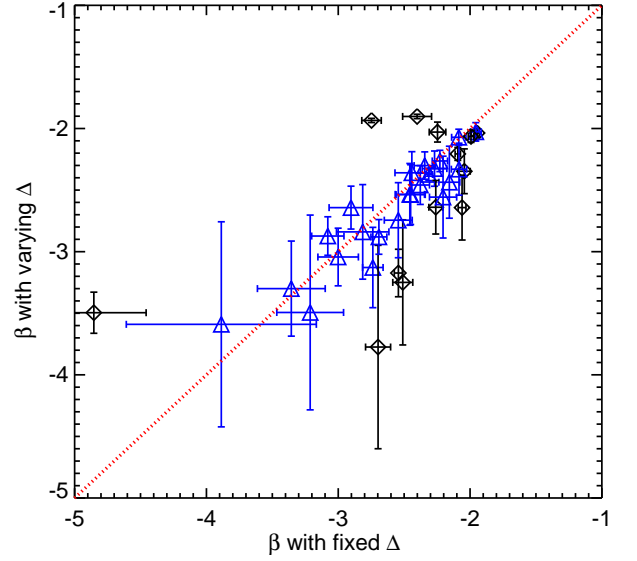


(a)

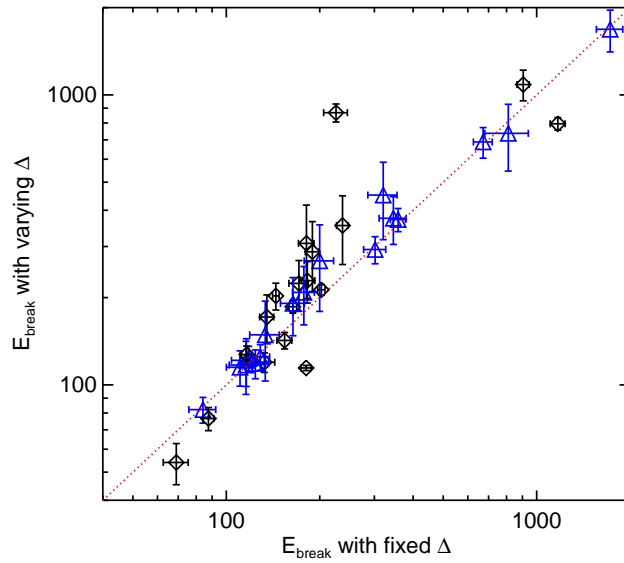
Fig. 17.— Distribution of the break scale  $\Delta$  of the SBPL  $F$  spectral fits.



(a)

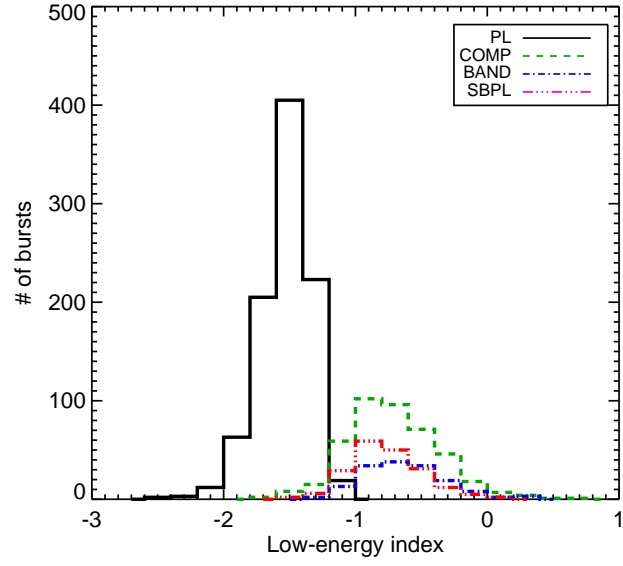


(b)

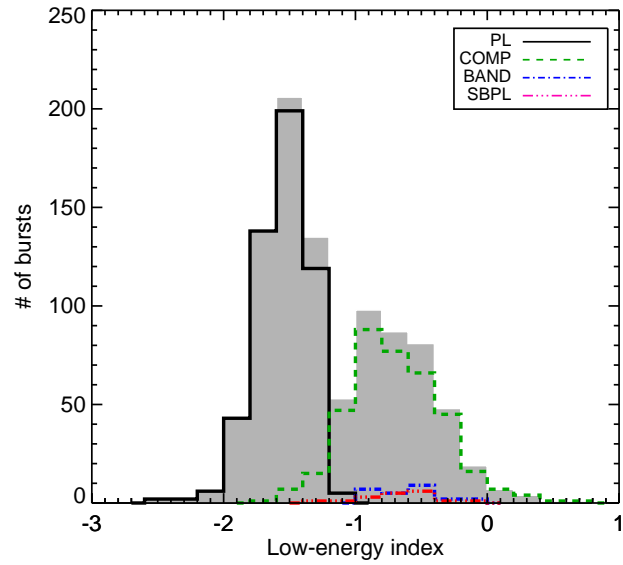


(c)

Fig. 18.— Comparison of SBPL model parameters with  $\Delta$  free to vary and fixed to 0.3. Values consistent within  $1\sigma$  (blue triangles) and not consistent within  $1\sigma$  (black diamonds) including a line of equality (red dashed line) are shown.

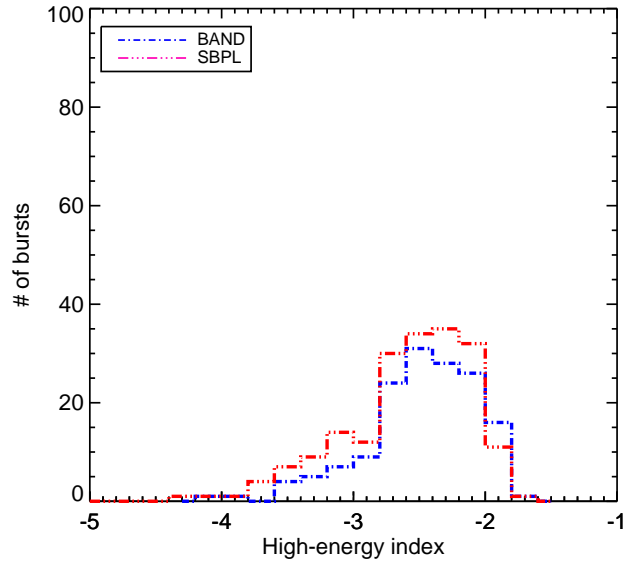


(a)

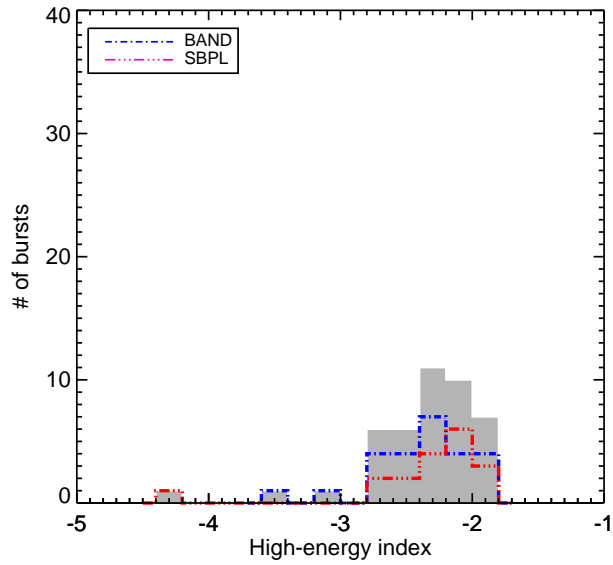


(b)

Fig. 19.— Distribution of the low-energy indices obtained from the GOOD  $P$  spectral fits (a). The BEST parameter distribution (gray filled histogram) and its constituents for the low-energy index is shown in (b).

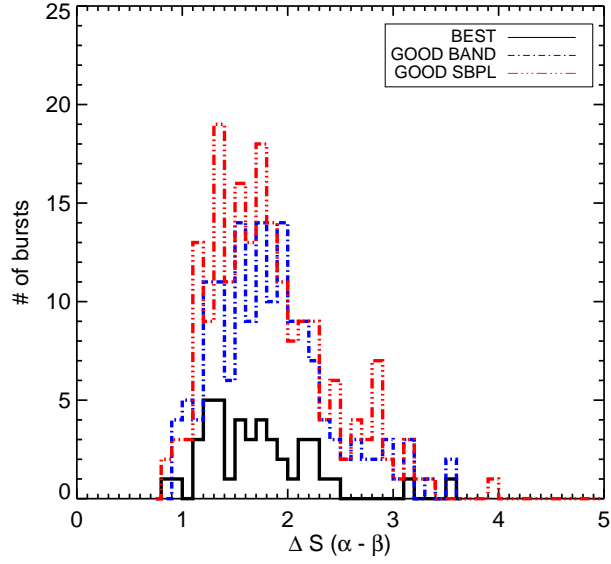


(a)



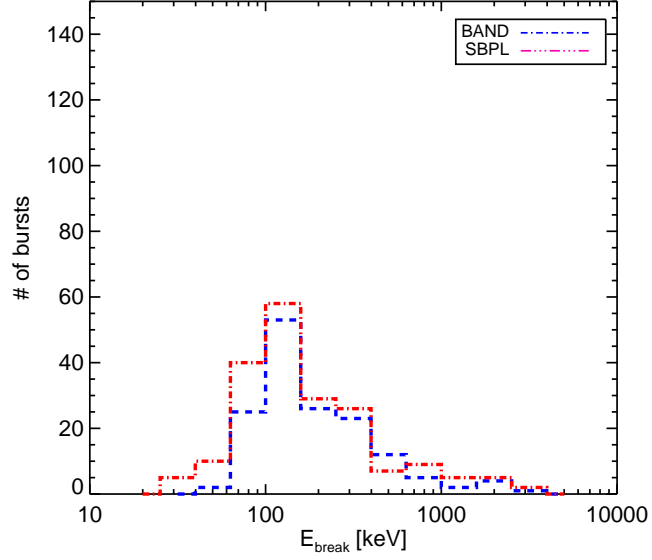
(b)

Fig. 20.— Distribution of the high-energy indices obtained from the GOOD  $P$  spectral fits (a). The BEST parameter distribution (gray filled histogram) and its constituents for the high-energy index is shown in (b).

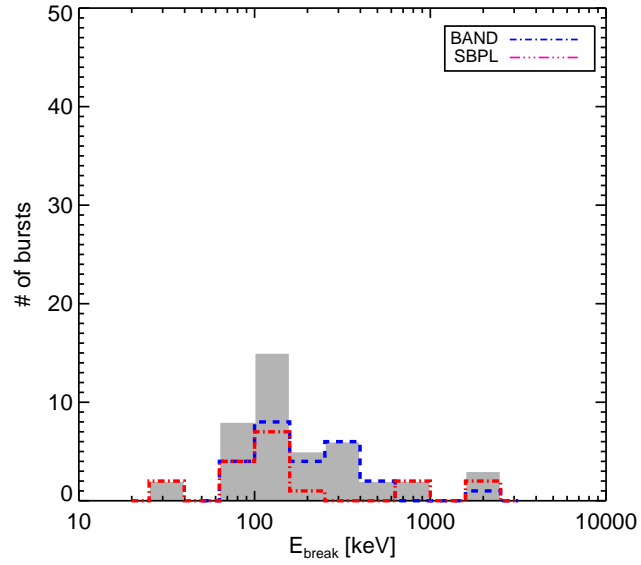


(a)

Fig. 21.— Distributions of  $\Delta S$ , the difference between the low- and high-energy spectral indices ( $\alpha - \beta$ ) for the  $P$  spectral fits. The BEST (black solid line), the GOOD BAND power-law indices (blue dash-dotted line) and the GOOD SBPL power-law indices (red dash-dot-dot-dotted line) for the  $F$  spectral fits are shown. The first bin contains values less than 0, indicating that the centroid value of  $\alpha$  is steeper than the centroid value of  $\beta$ .

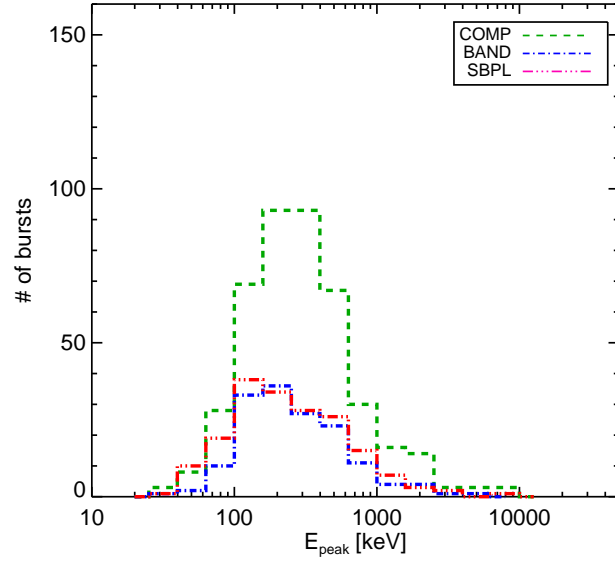


(a)

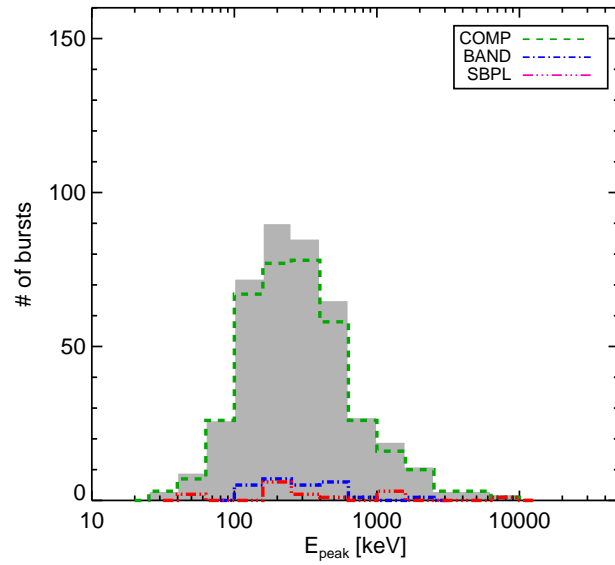


(b)

Fig. 22.— Distribution of the  $E_b$  obtained from the GOOD  $P$  spectral fits (a). The BEST parameter distribution (gray filled histogram) and its constituents for  $E_b$  is shown in (b).

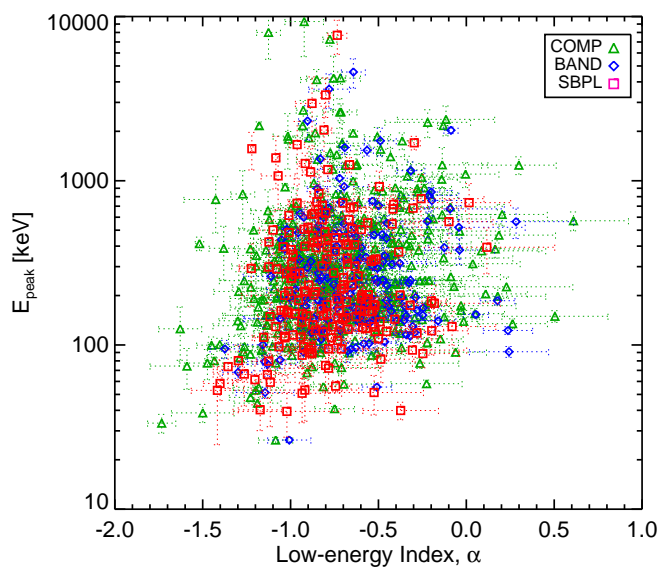


(a)

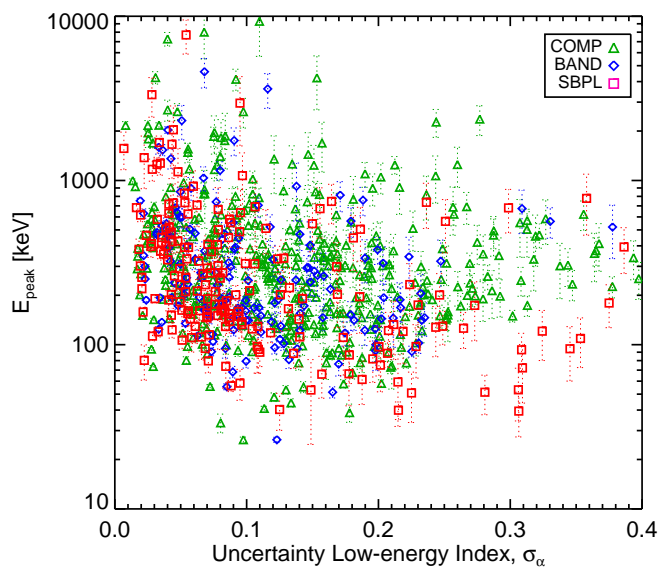


(b)

Fig. 23.— Distribution of the  $E_{\text{peak}}$  obtained from the GOOD  $P$  spectral fits (a). The BEST parameter distribution (gray filled histogram) and its constituents for  $E_{\text{peak}}$  is shown in (b).

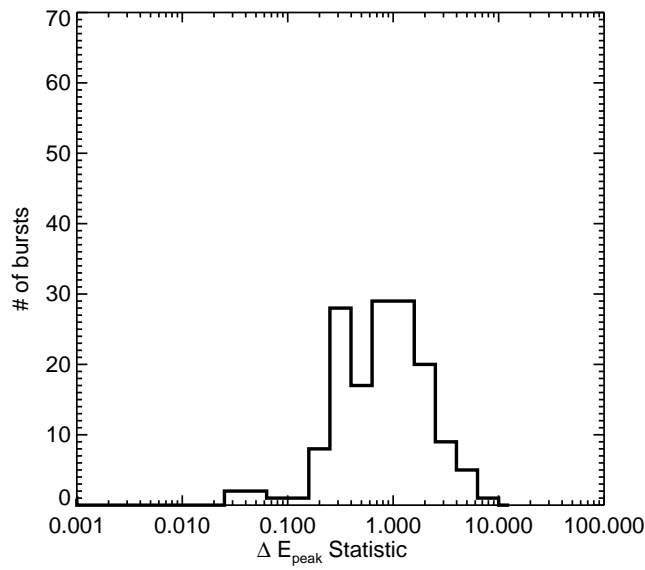


(a)



(b)

Fig. 24.— Comparison of the low-energy index and  $E_{\text{peak}}$  for three models from the  $P$  spectral fits. This comparison reveals a correlation between the  $E_{\text{peak}}$  energy and the uncertainty on the low-energy index: generally a lower energy  $E_{\text{peak}}$  tends to result in a less constrained low-energy index.



(a)

Fig. 25.— Distribution of the  $\Delta E_{\text{peak}}$  statistic for the COMP and BAND models from  $P$  spectral fits. A value less than 1 indicates the  $E_{\text{peak}}$  values are within errors, while a value larger than 1 indicates the  $E_{\text{peak}}$  values are not within errors.

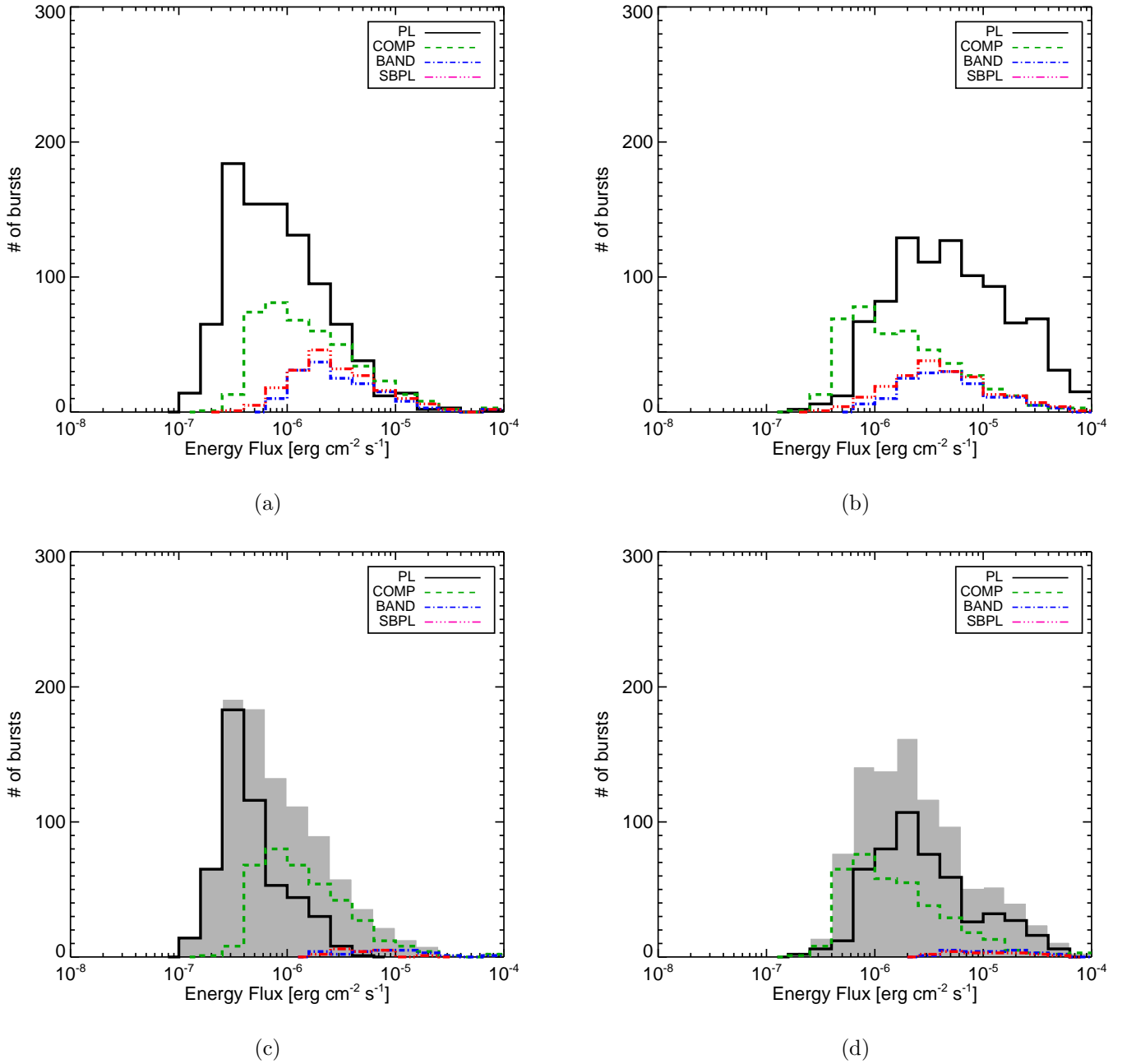


Fig. 26.— Distributions of energy flux in the 10 keV–1 MeV (a) and 10 keV–40 MeV (b) band from the GOOD  $P$  spectral fits. Note that the plotted distributions contain the flux on two different timescales: 1024 ms (long GRBs) and 64 ms (short GRBs). The BEST parameter distribution for the energy flux in both energy ranges is shown in (c) and (d). The gray filled histogram shows the total distribution and the constituents are shown in colors.

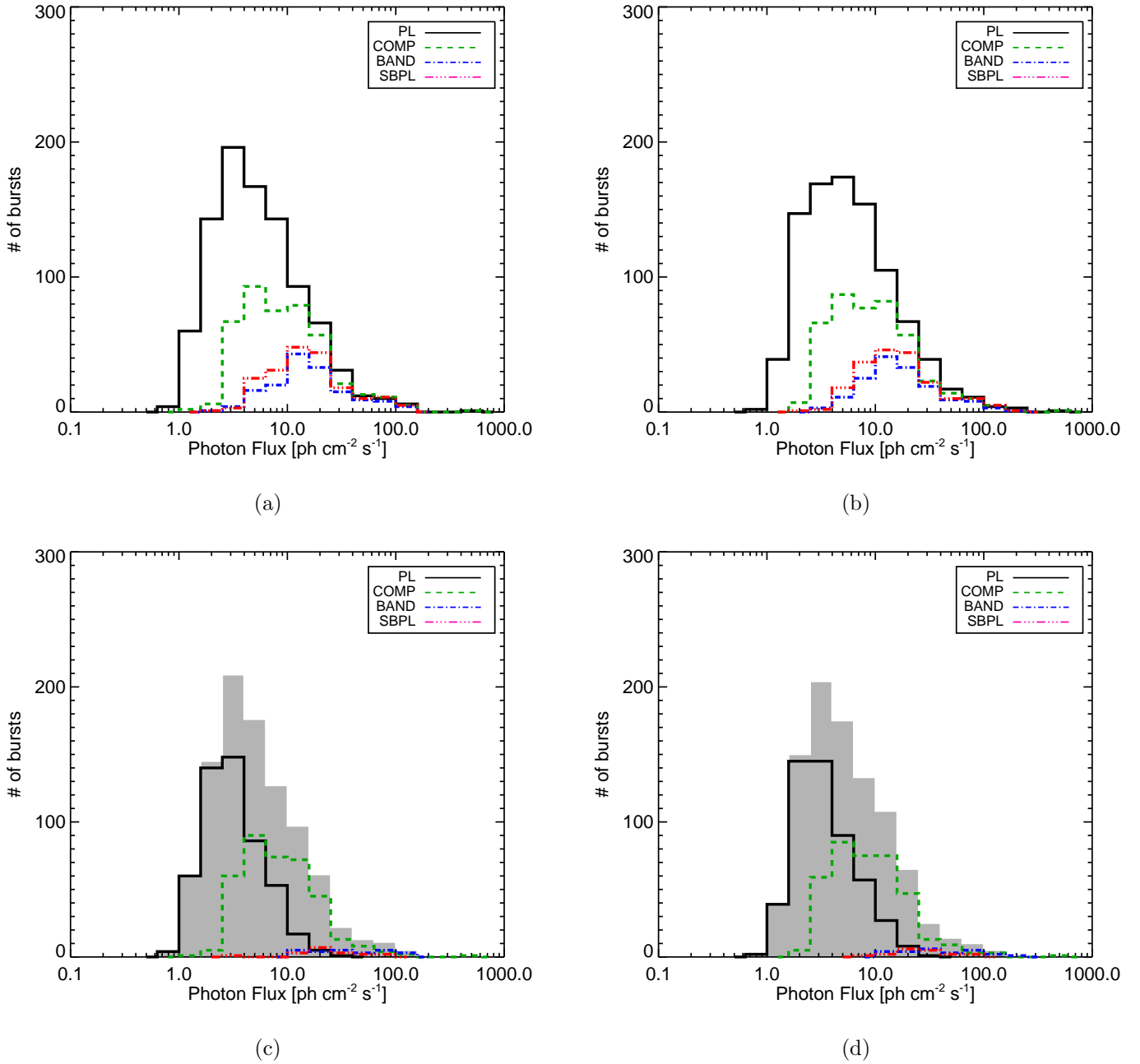


Fig. 27.— Distributions of photon flux in the 10 keV–1 MeV (a) and 10 keV–40 MeV (b) band from the GOOD  $P$  spectral fits. Note that the plotted distributions contain the flux on two different timescales: 1024 ms (long GRBs) and 64 ms (short GRBs). The BEST parameter distribution for the photon flux in both energy ranges is shown in (c) and (d). The gray filled histogram shows the total distribution and the constituents are shown in colors.

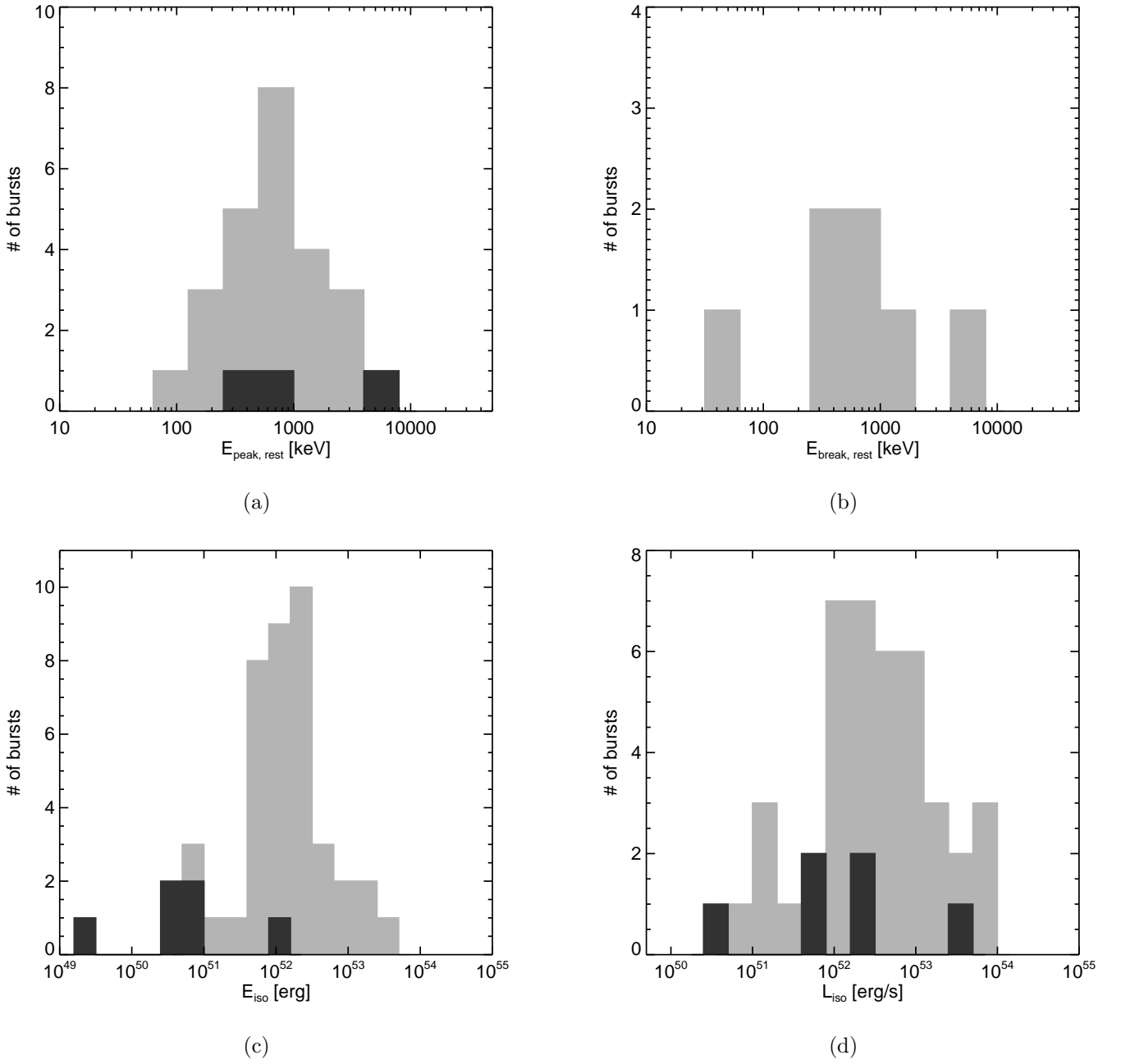


Fig. 28.— (a)  $E_{\text{peak}}^{\text{rest}}$  distribution of the  $P$  spectra fits from the BEST sample for long and short GRBs (light gray and dark gray filled histogram, respectively). (b) Same as (a) but for  $E_{\text{break}}^{\text{rest}}$ . (c) and (d) Distribution of  $E_{\text{iso}}$  and  $L_{\text{iso}}$  of the fluence spectral fits from the BEST sample in the rest-frame energy band  $1/(1+z)$  keV to  $10/(1+z)$  MeV.

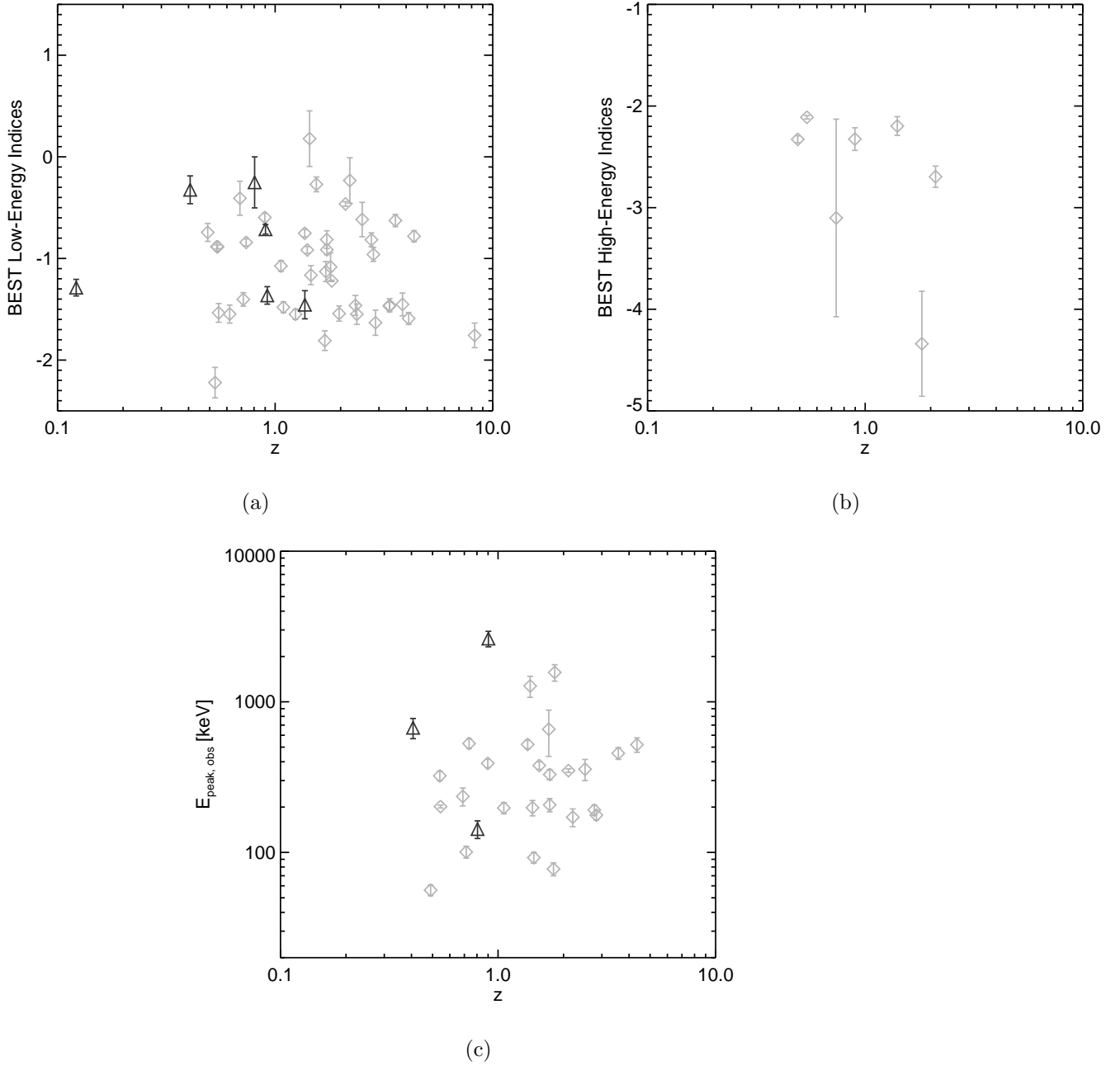


Fig. 29.— BEST spectral parameters as a function of the redshift of the  $P$  spectral fits for short (black triangles) and long (light-gray diamonds) GRBs.

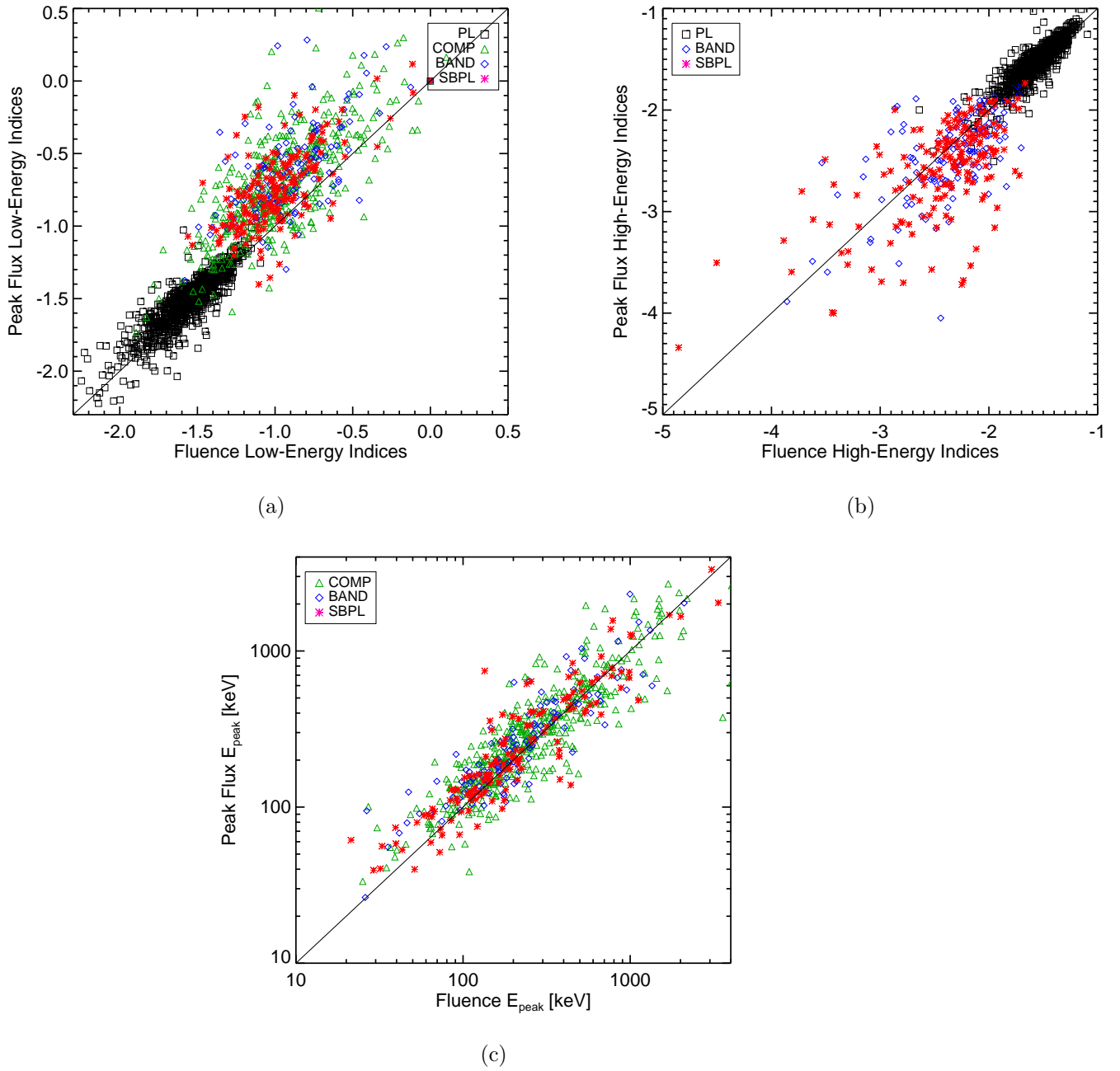
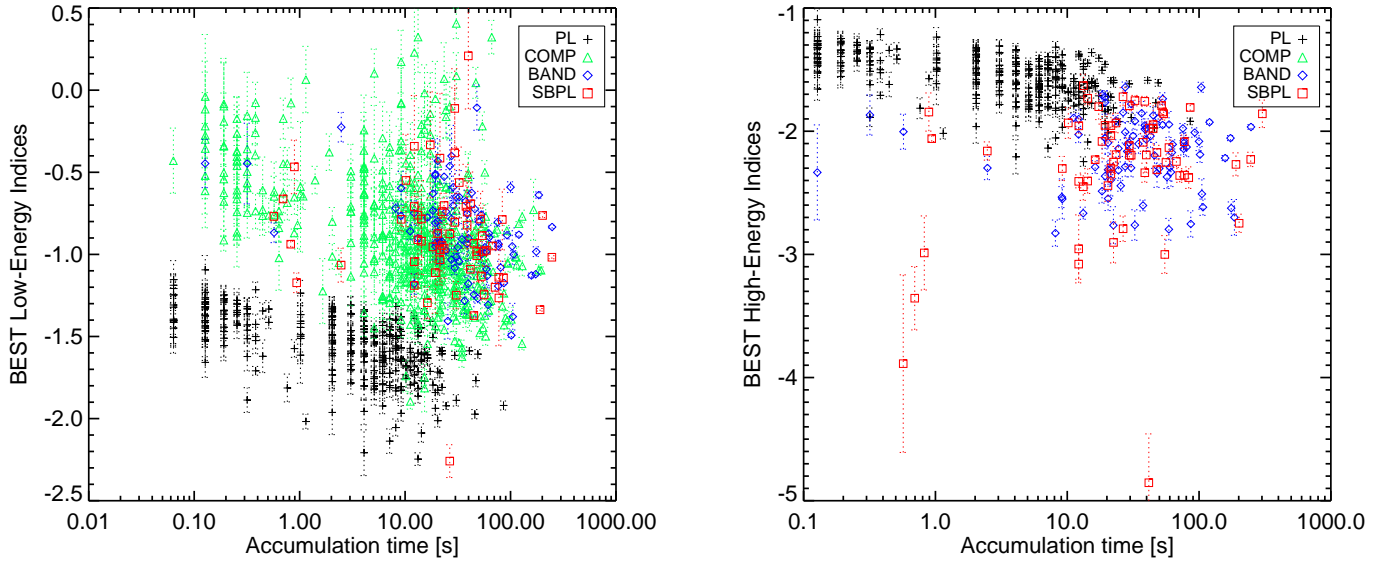
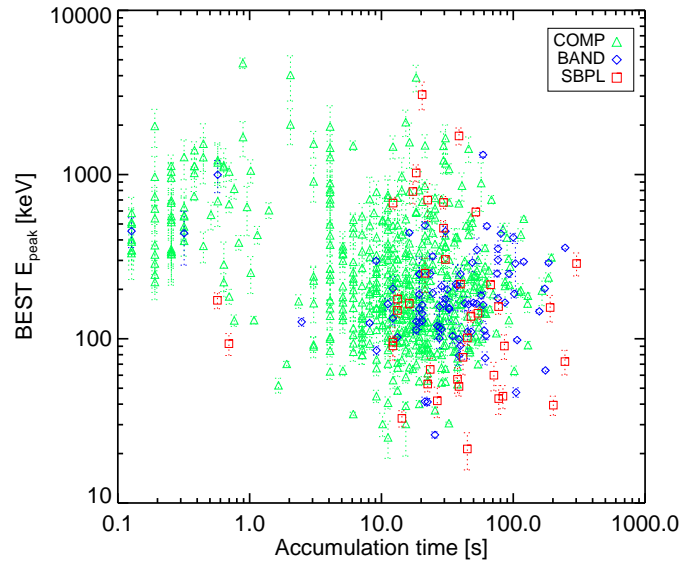


Fig. 30.—  $P$  spectral parameters as a function of the fluence spectral parameters for the GOOD sample. For all three parameters there is evidence for a strong correlation between the parameters found for the  $F$  spectra and those for the  $P$  spectra. Note that the PL index is shown in both (a) and (b) for comparison.



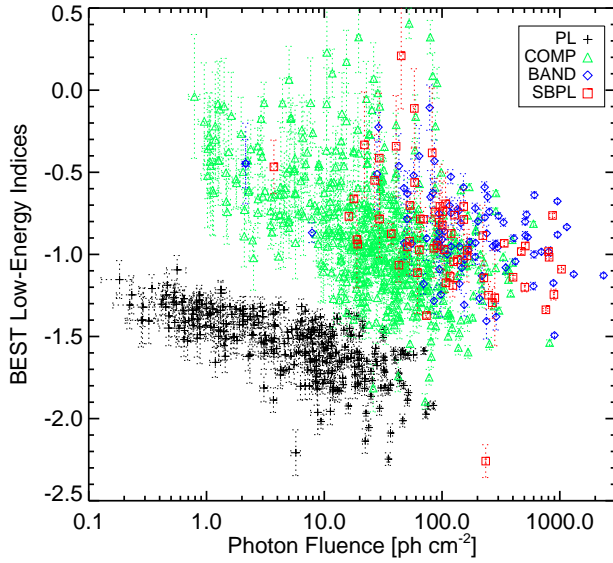
(a)

(b)

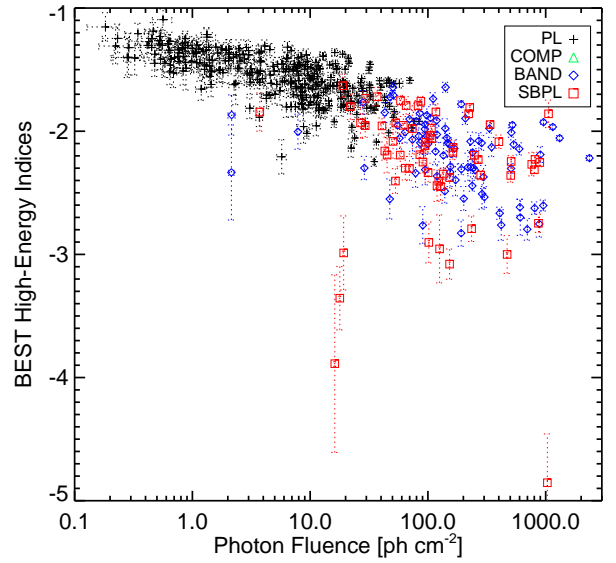


(c)

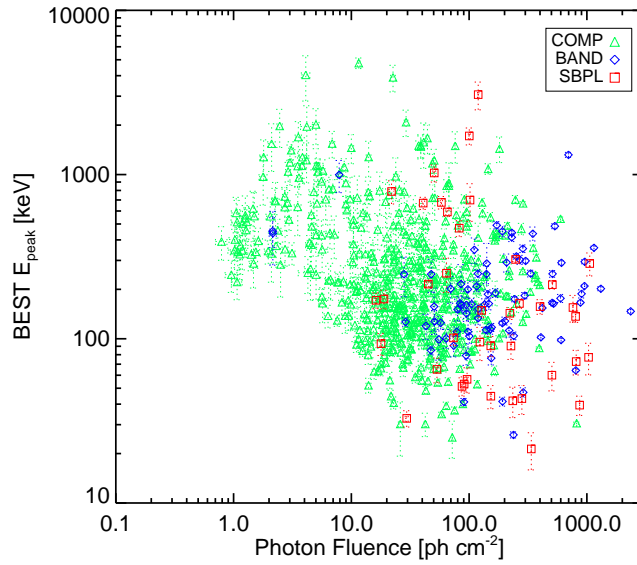
Fig. 31.— BEST spectral parameters as a function of the accumulation time for  $F$  spectral fits. Note that the PL index is shown in both (a) and (b) for comparison.



(a)

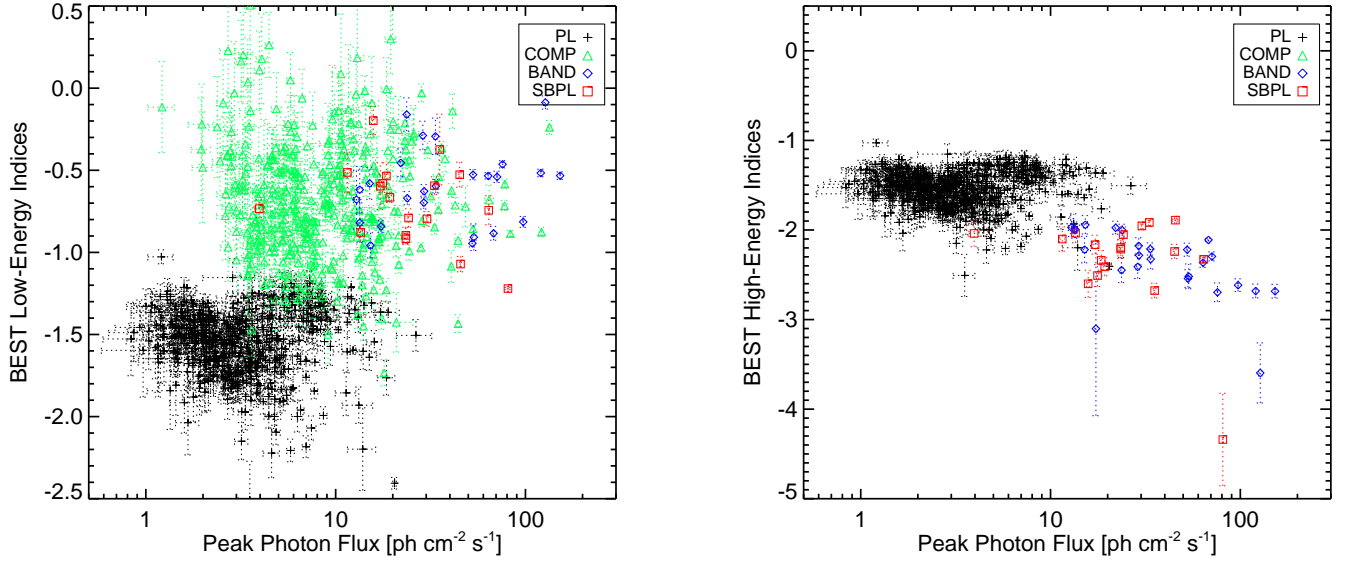


(b)



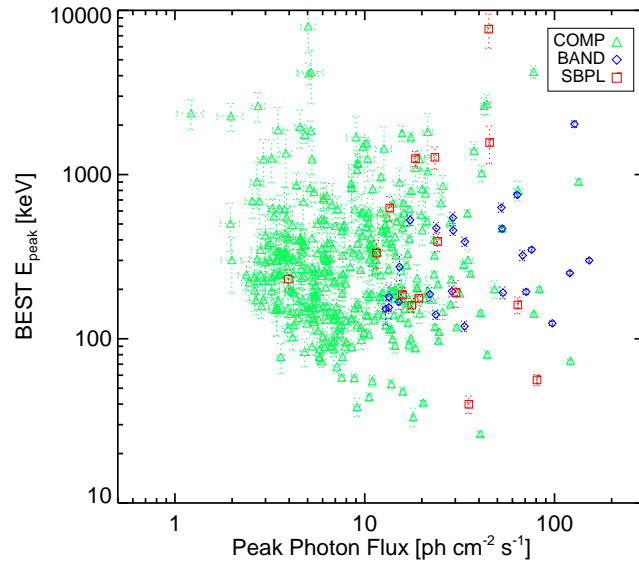
(c)

Fig. 32.— BEST spectral parameters as a function of the model photon fluence of the  $F$  spectral fits. Note that the PL index is shown in both (a) and (b) for comparison.



(a)

(b)



(c)

Fig. 33.— BEST spectral parameters as a function of the model peak photon flux of the  $P$  spectral fits. Note that the PL index is shown in both (a) and (b) for comparison.

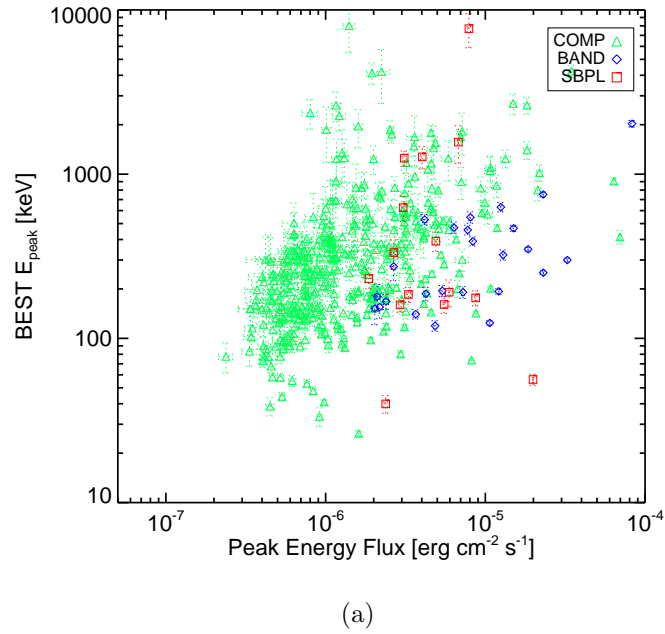


Fig. 34.— BEST  $E_{\text{peak}}$  as a function of the model energy flux of the  $P$  spectral fits.

Table 1. Determination of  $\Delta\text{C-Stat}_{\text{crit}}$

Burst	Fluence	$\Delta\text{C-Stat}_{\text{crit}}$	$\Delta\text{C-Stat}_{\text{crit}}$
	[erg]	PL vs. COMP	COMP vs. BAND
GRB 120608.489	5.2e-07	8.55	13.35
GRB 110227.240	1.9e-06	7.75	9.56
GRB 120129.580	5.8e-05	8.25	10.55
GRB 120526.303	1.3E-04	9.75	13.85
average	–	8.58	11.83

Table 2. BEST and GOOD GRB models.

	PL	SBPL	BAND	COMP
<b>Fluence Spectra</b>				
BEST	282 (29.9%)	62 (6.6%)	81 (8.6%)	516 (54.7%)
GOOD	941 (99.7%)	392 (41.5%)	342 (36.2%)	684 (72.5%)
<b>Peak Flux Spectra</b>				
BEST	514 (54.4%)	18 (1.9%)	25 (2.6%)	375 (39.7%)
GOOD	932 (98.7%)	196 (20.8%)	153 (16.2%)	430 (45.6%)

Table 3. The Median Parameter Values and the 68% C.L. of the Distributions of the GOOD Sample

Model	Low-Energy Index	High-Energy Index	$E_{\text{peak}}$ (keV)	$E_{\text{break}}$ (keV)	Photon Flux ( $\text{ph s}^{-1} \text{ cm}^{-2}$ )	Energy Flux ( $10^{-7} \text{ erg s}^{-1} \text{ cm}^{-2}$ )	$\Delta S$
<b>Fluence Spectra</b>							
PL	$-1.54^{+0.17}_{-0.20}$	-	-	-	$2.52^{+3.91}_{-1.11}$	$3.41^{+7.11}_{-1.48}$	-
COMP	$-0.96^{+0.37}_{-0.30}$	-	$211^{+333}_{-109}$	-	$2.53^{+4.22}_{-1.10}$	$3.19^{+8.55}_{-1.66}$	-
SBPL	$-0.98^{+0.28}_{-0.23}$	$-2.35^{+0.35}_{-0.52}$	$166^{+293}_{-82}$	$112^{+151}_{-55}$	$3.29^{+4.71}_{-1.54}$	$4.54^{+9.51}_{-2.40}$	$1.38^{+0.63}_{-0.37}$
BAND	$-0.86^{+0.33}_{-0.25}$	$-2.29^{+0.30}_{-0.39}$	$174^{+286}_{-73}$	$118^{+168}_{-41}$	$3.16^{+4.85}_{-1.55}$	$4.64^{+7.96}_{-2.50}$	$1.43^{+0.53}_{-0.39}$
BEST	$-1.08^{+0.43}_{-0.44}$	$-2.14^{+0.27}_{-0.37}$	$196^{+336}_{-100}$	$103^{+129}_{-63}$	$2.38^{+3.68}_{-1.05}$	$3.03^{+7.41}_{-1.40}$	$1.26^{+0.50}_{-0.32}$
<b>Peak Flux Spectra</b>							
PL	$-1.50^{+0.16}_{-0.20}$	-	-	-	$4.77^{+9.55}_{-2.69}$	$7.29^{+16.25}_{-4.25}$	-
COMP	$-0.75^{+0.38}_{-0.28}$	-	$270^{+370}_{-138}$	-	$8.49^{+12.79}_{-4.57}$	$13.19^{+32.57}_{-7.39}$	-
SBPL	$-0.79^{+0.27}_{-0.23}$	$-2.49^{+0.33}_{-0.64}$	$202^{+422}_{-105}$	$141^{+239}_{-63}$	$14.46^{+18.70}_{-7.74}$	$24.44^{+48.07}_{-13.77}$	$1.76^{+0.68}_{-0.46}$
BAND	$-0.64^{+0.32}_{-0.28}$	$-2.41^{+0.33}_{-0.46}$	$239^{+327}_{-116}$	$153^{+240}_{-54}$	$14.62^{+18.40}_{-7.81}$	$24.69^{+45.58}_{-13.02}$	$1.78^{+0.57}_{-0.47}$
BEST	$-1.32^{+0.74}_{-0.33}$	$-2.24^{+0.26}_{-0.38}$	$261^{+364}_{-130}$	$133^{+349}_{-39}$	$4.57^{+8.82}_{-2.49}$	$6.49^{+17.52}_{-3.46}$	$1.64^{+0.59}_{-0.36}$

Table 4. The Median Parameter Values and the 68% C.L. of the BEST Model Fits

Dataset	Low-Energy	High-Energy	$E_{\text{peak}}$	$E_{\text{break}}$	Photon Flux	Energy Flux
	Index	Index	(keV)	(keV)	( $\text{ph s}^{-1} \text{cm}^{-2}$ )	( $10^{-7} \text{erg s}^{-1} \text{cm}^{-2}$ )
<b>Fluence</b>						
This Catalog BEST	$-1.08^{+0.43}_{-0.44}$	$-2.14^{+0.27}_{-0.37}$	$196^{+336}_{-100}$	$103^{+129}_{-63}$	$2.38^{+3.68}_{-1.05}$	$3.03^{+7.41}_{-1.40}$
Goldstein et al. (2012)	$-1.05^{+0.44}_{-0.45}$	$-2.25^{+0.34}_{-0.73}$	$205^{+359}_{-121}$	$123^{+240}_{-80.4}$	$2.92^{+3.96}_{-1.31}$	$4.03^{+9.38}_{-2.13}$
Nava et al. (2011)	$-0.99^{+0.48}_{-0.49}$	$-2.33^{+0.17}_{-0.38}$	$174^{+320}_{-100}$	–	–	$2.26^{+9.48}_{-1.34}$
Kaneko et al. (2006)	$-1.14^{+0.20}_{-0.22}$	$-2.33^{+0.24}_{-0.26}$	$251^{+122}_{-68}$	$204^{+76}_{-56}$	–	–
<b>Peak Flux Spectra</b>						
This Catalog BEST	$-1.32^{+0.74}_{-0.33}$	$-2.24^{+0.26}_{-0.38}$	$261^{+364}_{-130}$	$133^{+349}_{-39}$	$4.57^{+8.82}_{-2.49}$	$6.49^{+17.52}_{-3.46}$
Goldstein et al. (2012)	$-1.12^{+0.61}_{-0.50}$	$-2.27^{+0.44}_{-0.50}$	$223^{+352}_{-126}$	$172^{+254}_{-100}$	$5.39^{+10.18}_{-2.87}$	$8.35^{+22.61}_{-4.98}$
Nava et al. (2011)	$(-0.56^{+0.40}_{-0.37})^{\text{a}}$	$-2.39^{+0.23}_{-0.62}$	$225^{+391}_{-122}$	–	–	$13.5^{+79.8}_{-10.1}$
Kaneko et al. (2006)	$-1.02^{+0.26}_{-0.28}$	$-2.33^{+0.26}_{-0.31}$	$281^{+139}_{-99}$	$205^{+72}_{-55}$	–	–

<sup>a</sup>Low-energy index of the peak flux spectra with curved function only.